Perovskite memristors for energy efficient computing

INVESTIGATION OF THE RESISTIVE SWITCHING PROPERTIES IN 3-DIMENSIONAL AND 2-DIMENSIONAL ORGANIC-INORGANIC HALIDE PEROVSKITE DEVICES

THESIS MSC PHYSICS & ASTRONOMY

Author:

Oscar VAN DE WATER

Studentnumber:

11334746

Date:

July 14, 2022

Supervisor:

Prof. Dr. Bruno EHRLER

Examiner:

Prof. Dr. Erik GARNETT

Daily Supervisor:

MSc Jeroen DE BOER

UNIVERSITEIT VAN AMSTERDAM

Abstract

Neuromorphic engineering will play an essential part in the integration of hardware for ultra-fast and highly energy efficient processing and storage of data. In order to realize this, research for computing is focused on emulating the biological brain, which contains an amount of 10^{11} highly densely integrated neurons, parallelly connected via synapses. In neuromorphic computing systems and artificial synapses, both the storage and processing of data is done in-situ, which cuts the need for data to be moved around an electrical circuit. This results in faster and more energy efficient computations than conventional computing systems. In order to achieve in-memory computing, passive circuit elements that can change their resistance in response to electrically induced stresses are needed. These materials and devices are called memristors, because they 'remember' what current has previously flown through the device in response to an electric field. One of the most promising emerging materials with memristive properties are organic-inorganic metal halide perovskites (MHP), which can change their resistance due to intrinsic stability issues, resulting in the migration of charged ions through the crystal structure. The efficient conduction of ions causes Current-Voltage (IV) hysteresis, which makes MHP's interesting for memory switching devices and artificial synapses. The exact mechanisms behind the resistive switching effect in MHP's is to date not fully understood. There are numerous parameters that influence the switching effect, and similar perovskite structures show very different results. In this thesis, we investigate the resistive switching properties of $MAPbI_3$ 3D and PEA_2PbI_4 2D MHP thin films and present the difference their differences in energy consumption, conductive states and endurance. We will also discuss what mechanisms might be the origin of the switching effect in these devices. Furthermore, we will examine the influence of the addition of an organic hole-transport material within the device stack on the resistive switching effect. Research was conducted by characterizing the perovskites with XRD, AFM and SEM. Fabricated devices were measured with IV sweeps and Pulsed Voltage Stresses (PVS). The main findings show a clear difference in the memristive switching properties between the 3D and 2D perovskites, where 2D perovskites show lower operating currents (factor $< 10^1$), higher ON/OFF ratios (factor $> 10^1$) and potential lower power consumption upon operation (factor $< 10^2$) compared to 3D perovskites. However, the resistive switching in 2D perovskites is not always reproducible over all cycles, making the 2D perovskite devices more stochastic in their memory behaviour. The addition of the hole-transport material improves overall ON/OFF ratio and endurance of the devices, making it a very promising candidate for further research. These results show the difference resistive switching behaviour due to ion migration in MHP's. However, more in-depth research is needed to obtain a clear picture of the switching mechanisms due to ion migration in MHP thin films.

Contents

1 Introduction **5**

1.1 Beyond the von Neumann Bottleneck 5

1.2 Metal Halide Perovskites for in-memory computing 6

1.3 Research topic 7

2 Theoretical Framework **8**

2.1 Artificial Synapses 8

2.1.1 Neuromorphic Computing 8

2.1.2 Memristors 11

2.2 Perovskite materials 15

2.2.1 3D and 2D perovskites 15

2.2.2 Ion migration 16

2.3 2D/3D Perovskite Artificial Synapses 18

2.3.1 Interfacial (doping) effects 18

2.3.2 Conductive filament formation 21

2.3.3 Device structure in this research 22

3 Methodology **24**

3.1 Preparation of thin films 24

3.1.1 Cleaning ITO coated substrates 24

3.1.2 PTAA bottom transport layer 24

3.1.3 Perovskite thin film 24

3.1.4 Spiro-OMeTAD top transport layer 25

3.1.5 Au top contact layer 25

3.2 Characterization 25

3.2.1 Material Characterization 25

3.2.2 Device Characterization 26

4 Results and Discussion **27**

4.1 Characterization of thin films 27

4.2 3D versus 2D 31
4.2.1 IV curves 31
4.2.2 Endurance measurements 33
4.3 Addition of Spiro-OMeTAD transport layer 35
4.3.1 IV curves 35
4.3.2 Endurance measurements 36
4.4 Pulsed Voltage Stresses 38

5 Conclusion 40

6 Acknowledgements 42

7 References 43

8 Appendix 51
8.1 Bottom layers characterization 51
8.2 Spiro-OMeTAD top layer characterization 52
8.3 Extra IV sweeps 53
8.4 Endurance 54

1. Introduction

Greenhouse gas emissions by human activity has caused the average global temperature to rise past 1 °C compared to pre-industrial levels. Extreme measures are needed to prevent average temperatures to quickly pass the 1.5 °C set limit by the Paris climate agreement in 2015.[1] An essential part of reaching these set goals is shifting away from fossil fuels and generating sustainable energy. However, annual global energy consumption keeps rising, making this task even more difficult.[2] A sector that increasingly demands more energy is the digital technology sector. Over the past few decades, computer science has rapidly developed by the implementation of artificial intelligence, including machine learning algorithms and artificial neural networks.[3] With the wide deployment of deep learning, the main focus of development is on functionality, reliability and accuracy, but not on energy efficiency.[4] Currently, the global energy consumption of data processing demands more than 400 terawatt hours (TWh) of energy per year,[5] forecast to increase to more than 3,000 TWh by 2030.[6] A master plan is needed to find alternative approaches to drastically lower the energy consumption of data processing and transfer.

1.1. Beyond the von Neumann Bottleneck

Conventional computer systems operate by sending data back and forth between the central processing unit (CPU) and the memory unit, where the data is stored. Current electronics separates these components, which results in data being transferred back and forth through the circuit. The physical separation between processing and memory unit is known as the Von Neumann computer architecture.[7] The increasing amount of data transfer between the memory and processing unit leads to high energy consumption and latency, limiting the system towards the 'von Neumann Bottleneck'.[8] To address the shortcomings of this conventional system, research takes inspiration from biological systems. A typical human brain contains 10^{11} neurons, which have 10^4 connections to each other by 10^{15} synapses.[9] This highly dense integrated system uses around 20 W of power to perform daily computational tasks. Digital simulations of artificial neural networks of the same network size consume 7.9 MW, which is a difference of 6 orders of magnitude.[10,11] Reaching the ultra low energy consuming computations of the brain (1-100 femtoJoule per synaptic event) is one main objective of research in neuromorphic computing. In neuromorphic computing systems, both the storage and processing of data is done in-situ, which cuts the need for data being moved around an electrical circuit. This allows for faster, more complex and more energy efficient operations. In-memory computing systems are estimated to train neural networks with a two order of magnitude gain in terms of energy consumption and speed com-

pared to conventional processing cards.[12] Exploration of novel materials and devices that have a memory effect in their conductance will be needed to advance the field of in-memory computing. Investigated material classes range from magnetic alloys, metal oxides to chalcogenides and 2D van der Waals materials.[7,13,14] Also organic materials show a very promsing memory effect, where sub-femtojoule levels have already been reported.[15] However, their thermal instability and the lack of a well-defined memory effect are disadvantageous for applications. The field of neuromorphic computing is looking further to find promising sustainable materials for in-memory computing with ultra-low energy consumption and high stability.

1.2. Metal Halide Perovskites for in-memory computing

Metal halide perovskites (MHP) have rapidly emerged as a semiconducting material in academic research in the last decade. MHP's have an interchangeable composition of organic and inorganic ions in their crystal structure, which enables tunability of the bandgap and charge transport through the material. These properties make them very interesting for the application in solar cells and light emitting diodes.[16] Also, production process of MHP's is potentially cheap, as it is based on low-temperature solution-based fabrication.[17] This enables large-scale, low-cost manufacturing of perovskites as an optoelectronic material. However, perovskites tend to be unstable in ambient conditions due to their sensitivity to moisture, oxygen and heat, hindering its application on an industrial level.[18–20] Moreover, defect formation within the crystal lattice of MHP's results in current-voltage hysteresis. Favorably modulating the detrimental hysteretic effect in solar cells makes MHP's interesting for memory switching devices and artificial synapses.[21,22] In perovskite artificial synapses, the migration of ions is used to change the resistance of the device. Recently researched perovskite-based memory devices have demonstrated high data storage density, low power consumption and fast conductance switching, out-competing conventional oxide-based switching memories.[22–26] There are different mechanisms proposed in perovskites that change the electrical conductance in the material. Due to the research in the wide range of perovskite compositions being in its infancy, it is still under debate which of these effects are taking place. More investigation is needed to understand and optimize the memory behaviour in perovskite-based devices for artificial synapses.

1.3. Research topic

This thesis focuses on investigating different architectures of organic-inorganic MHP's devices to obtain a better understanding on the difference in resistive switching effects. We will compare these structures on the resistive switching behaviour and energy consumption. For further theoretical background, section 2.1 will explain neuromorphic computing, memristive switching mechanisms and the important properties of measuring memristive switching devices. Section 2.2 will explain the ionic-electronic properties in different perovskite compositions, followed by how these differences influence the memristive effect in these materials in section 2.3. The goal of this thesis is to demonstrate the device performance of different perovskite structures with the addition of organic transport layers, and to gain a better understanding of perovskite materials for artificial synapse applications. The methods used for this research are presented in Section 3 and subsequently the results are discussed in Section 4.

2. Theoretical Framework

2.1. Artificial Synapses

In this section, we start off with a broad theoretical framework needed to explain how artificial synapses work. First, the concepts and analogies of neuromorphic systems are explained. Then, the functioning of materials that have a variable resistance, i.e. the memristors, are highlighted. We further explain how mechanisms change the overall resistance of a memristive device and what parameters and properties are important to have a high performing memristor. At the end, we will highlight how perovskites have performed so far on these properties.

2.1.1. Neuromorphic Computing

'Neuromorphic' engineering, which literally means 'nervous (system) structure' engineering, inspires from the biological brain to alternatively store, process and compute data. In biology, the storage and processing of data is computed 'in-situ', where neurons send information parallel to each other by connected synapses. This process emerges from synapses that have short-term behavior for computations and long-term behavior for learning and memory.[27] The strength or weight of a the synaptic connection determines how well information is transferred to the next neuron. Synapses have the ability to change their strength, which allows it to have long-term behaviour as a memory component.[28] The parallel structures of the biological brain can therefore with extreme precision and efficiency compute data with variable weights. Within neuromorphic computing, similar functionality is attempted to be built by modelling and building electrical circuits with analogue electronic devices. These systems can have different approaches, like analogue data processing, parallel information processing or spiking-based information computing.[4] The most important emulation process in neuromorphic computing is the co-location of storage and processing of data, which needs electronic materials and devices which have similar memory behaviour as synapses and neurons. In order to emulate long-term synaptic behaviour, electronic devices are needed that have a variable resistance as a function of their history. Materials that have these properties are calles memristors. Their complex variable response to an electrical pulse allows them to be used as memory elements or variable weights in artificial synapses.[4]

The integration of memristors in electronic circuits will emulate the weights that synapses have in a biological system, and use these to form an analog signal. Memristors function as the artificial synapse, where the connected top electrode sends an input signal is the 'pre-synaptic neuron' and the bottom electrode that receives the output signal from the memristor is the 'post-synaptic neuron'. Multiple connected memristors can together be placed in an array of neurons, which will allow for the parallel memory and processing upon an electrical input signal.[7,29,30] Different architectures of these systems have already been proposed. A classical example is by engineering matrix-vector multiplication (MVM) arrays, which is a well-explained analogy to compute data as biological neural networks. Figure 2.1 shows the emulation of sending information via neuromorphic compution in a MVM array. Via MVM multiplication, every value in output vector Y_m can be calculated by separately multiplying each component of input vector x_n with the values w_{mn} within the column m, and summing over all the different multiplications. As an example, the first value Y_1 in the output vector would be calculated by subsequently multiplying the components of the vector x_n with the components in the first row w_{1n} of the matrix via

$$Y_1 = \sum_{i=1}^{n} (w_{11}x_1 + w_{12}x_2 + w_{13}x_3 + \ldots + w_{1n}x_n) = \sum_{i=1}^{n} w_{1i}x_i \tag{2.1}$$

Values Y_2, Y_3, ... , Y_m can be calculated via equation 2.1 in a similar way, together resulting in output vector

$$Y_m = \sum_{i=1}^{n} w_{mi}x_i \tag{2.2}$$

Within an MVM array architecture, the input vector V_n works as different voltage bias values on the top electrode, which can be seen as the pre-synaptic neuron. The conductance values are together formed by a matrix of memristors G_{mn}, similar to synapses that have variable weights. The output vector I_m is the different currents that have flown trough the device and is analogous to the pos-synaptic neuron.[3,31] Therefore, equation 2.2 can be physically expressed in neuromorphic circuit array to

$$I_m = \sum_{i=1}^{n} G_{mi}V_i \tag{2.3}$$

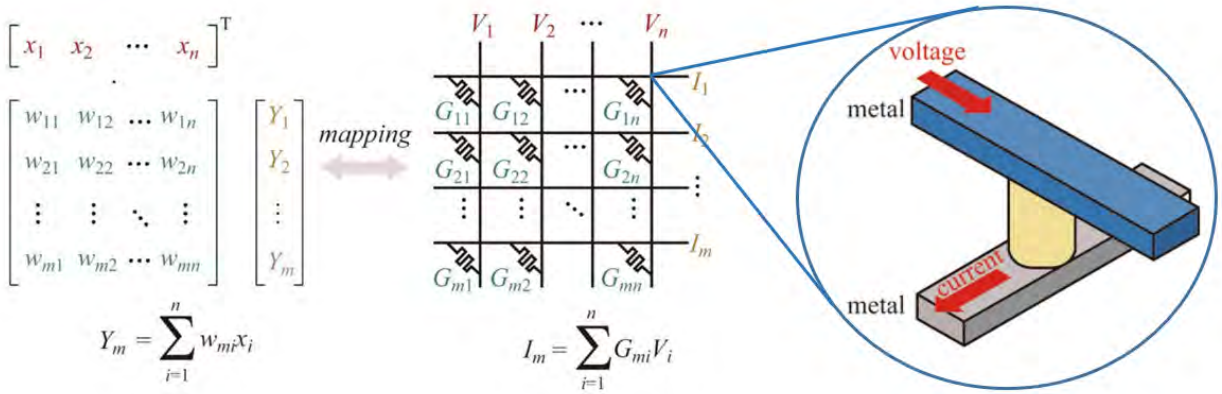

Fig. 2.1: left: matrix vector multiplication with vector x_n, matrix of weights w_{mn} and determined output vector Y_m. middle: An MVM array that computes electrical information similarly by exploiting Ohm's law and Kirchhoff's law: input voltage values V_n, matrix of memristors G_{mn} and output currents I_m. right: Schematic of physical representation of one component of an MVM array, where the yellow area is the memristor. From Reference.[3]

The physical explanation of equation 2.3 comes forth from both Ohm's law and Kirchoff's law. The output current of each component in the array can be determined by Ohm's law. This is simply the product of G_{mi} and the biased voltage V_i. Kirchoff's law determines the total output current at the bottom electrode, which is accumulated by adding the products of G_{mi} and V_i together, resulting in I_m.[29] The memory behaviour is within the matrix of weights w_{mn}, which will update their weight values depending on the current that has flown through them. A matrix of variable conductive states G_{mn} is therefore needed to perform the in-memory computing. Therefore, memristors fulfill these requirements and are promising to implement in neuromorphic systems. In the next section, we will explain how memristors work and what their important properties are.

2.1.2. MEMRISTORS

Memristors are passive circuit elements that can change their conductance in response to electrically induced stresses. The previously applied voltage determines the state of the resistance, which makes memristors devices that 'remember' what current has previously flown through it.[32] Figure 2.2 shows a schematic example of IV characteristics of a memristor device, measured under a direct-current (DC) voltage sweep. Starting at 0V in the positive bias (red), the current is initially low at low voltages. This stage is called the OFF state. At a certain threshold voltage, the current drastically increases to an ON state, where much higher currents are measured compared to the OFF state. When the voltage is decreased, the current stays high, which implies the device stays in its high resistive state. In negative bias, the device is still in the ON state, until it drops at a certain voltage back to the OFF state.

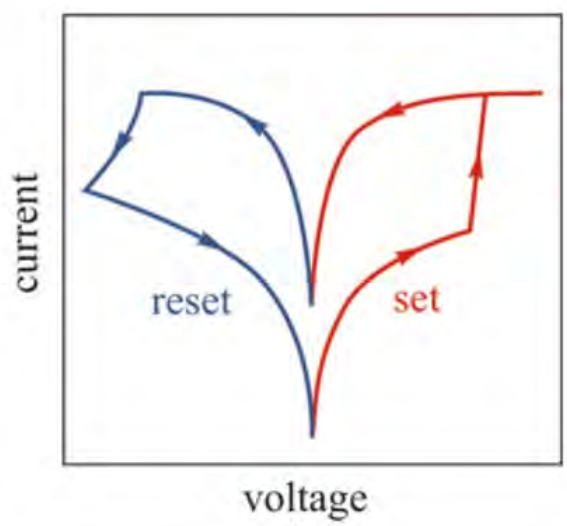

Fig. 2.2: Schematic of an example IV-characteristic of a memristor from reference.[3] In positive bias the SET (in this thesis ON switching) is the point where the current drastically increases. The RESET (OFF switching) is the point where the measured current rapidly decreases, allowing for different conductive states.

Research has shown that different mechanisms can take place in the active layer of the memristive materials, ranging from ferroelectricity[33] to atomic rearrangement that modulate the conductivity. Among the devices that show atomic rearrangement, there are 'analog memristors' that gradually change their conductance upon an increasing voltage bias. The origin of this conductive change is an interfacial doping effect between different regions in the material (Figure 2.3a).[34,35] There are also binary memristors, which show abrupt changes in their conductance at a threshold voltage by conductive filament formation between the two electrodes (Figure 2.3b).[36,37]

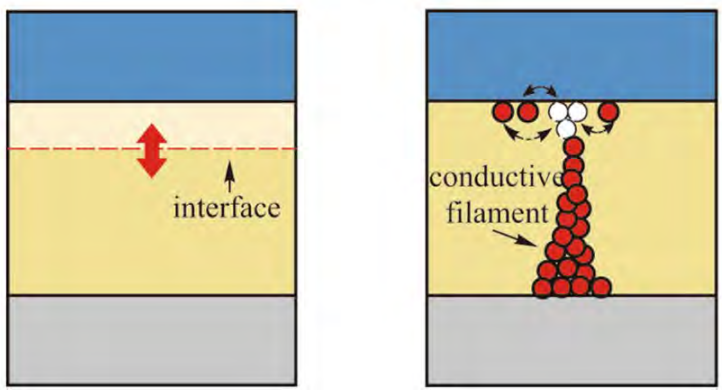

Fig. 2.3: Schematics of the two different atomic rearrangements lead different resistive switching mechanisms in a memristor. a) interfacial doping. b) conductive filament formation.[3]

A proposed model by Serrano-Gotarredona et al.[38] explains very well how these different mechanisms result in a change of the overall resistance. The first is the 'moving wall model' in Figure 2.4a. By interfacial doping effect in the material, a memristor of height L is divided into two regions. The boundary between the two regions is at the height w, which can change its position depending on the charge that has flown through the memristor. This boundary is the interface between the doped region w, which has a has low resistance R_{ON}, and the undoped region L - w, which has a high resistance R_{OFF}. The overall variable resistance of the whole memristor is the addition of both R_{ON} and R_{OFF} connected in series, therefore its memristive behaviour can be described by

$$R_{MR} = R_{ON}\frac{w}{L} + R_{OFF}\left(1 - \frac{w}{L}\right) \tag{2.4}$$

For the filamentary formation mechanism, multiple filaments can grow between two electrodes 2.4. The variable number and width of the filaments influences how much of the cross-sectional area S of the memristor is covered by effective conductive filaments w. The filaments with cross-sectional area w have the lower resistance R_{ON}, while the bulk of the memristor has high resistance R_{OFF}. Now the total resistance of the memristor behaves as two variable resistors connected parralel, therefore its memristive behaviour can be described by

$$\frac{1}{R_{\mathrm{MR}}} = \frac{1}{R_{\mathrm{ON}}}\frac{w}{S} + \frac{1}{R_{\mathrm{OFF}}}\left(1 - \frac{w}{S}\right) \tag{2.5}$$

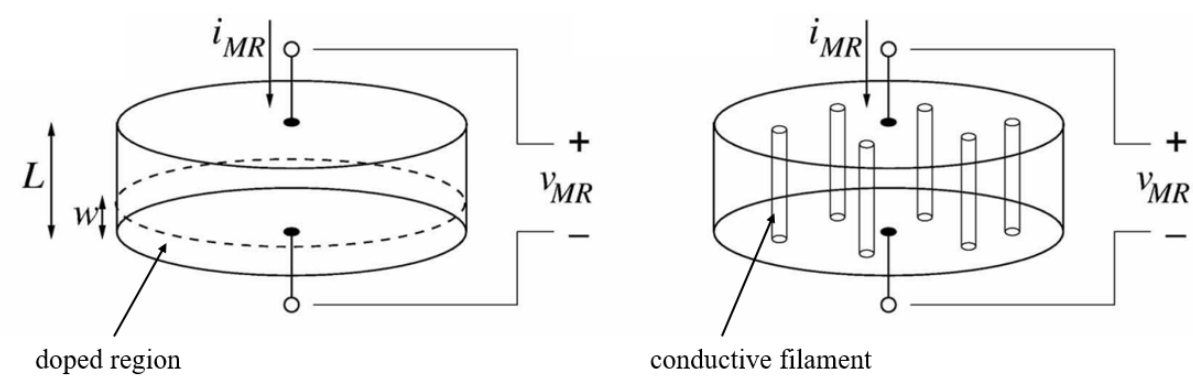

Fig. 2.4: a). Schematic of how atomic rearrangement leads to the formation of doped (w) and undoped (L-w) regions that are modeled as two variable resistors in series. b). Schematic of atomic rearrangement leading to filament formation in the material, resulting in multiple variable resistors operating in parralel.[38]

Emerging memristor materials are tested with different reliability tests to check if they can potentially be implemented in neuromorphic systems. Functional reliability of a memristor is determined by the precision, energy consumption and endurance of setting its resistive state. Degradation of the ratio between the high resistive state R_{ON} and low resisitive state R_{OFF} (from here onwards called the ON/OFF ratio) or inconsistent ON/OFF ratios make it difficult to target the input voltage bias accurately to set the memristor in the desired resistive state. Furthermore, a low ON/OFF ratio will make it difficult to accurately distinguish the difference in conductive states, which negatively influences the training accuracy of the memristor.[31] Therefore, a consistent and high ON/OFF ratio is important to track the precision of the memristor during the test. Other important parameters are the operating current (I), the operating voltage (V) and the time it takes for a mem-

ristor to switch between its ON and OFF states (t). These properties directly influence the electrical energy consumption of the memristor, described by

$$E = Pt = VIt \tag{2.6}$$

With this simple equation, the operating energy consumption can be calculated by multiplying the measured current with the applied voltage pulse amplitude and the pulse width.[13] Lowering these parameters to the lowest possible value will result in the lowest energy consumption for switching the resistive state of the memristor. Endurance of the memristive behaviour of the device is important to know after how many switching events the device 'breaks'. The breakpoint is defined if the memristor irreversibly loses its high ON/OFF ratio and low energy consumption. Measuring the endurance of a memristor device is difficult, because it is not always known how to induce the switching effect between the ON and the OFF state. This depends on what mechanism induces the switch, what magnitude of voltage pulse is needed, and how long this pulse is needed to induce the switching effect.[39,40] Therefore, research on memristive devices still portrays the switching effect via IV characteristics. However, the pulse-based voltage bias technique is used for realistic device computations to efficiently tune the memristive state of the device.[40]

Within the last 5-10 years of research of halide perovskite memristors, significant progress has been made on optimizing the energy efficiency and accuracy switching between states. The tunability of the bandgap is an essential parameter that affects the Schottky barrier height, therefore influencing the resistive switching effect. Halide perovskites have demonstrated low-energy operation, high ON/OFF ratios and mulitple switching states in combination with fast operation speed.[41] So far, the lowest reported current values are as low as 10^{-11} A, where most ON/OFF ratios are higher than 10^3.[42] Furthermore, reported V_{appl} values are as low as 10^{-1} V, which also improves the energy efficiency of the operating device. The highest reported ON/OFF ratio is 1.9 x 10^9 for a FTO/c-TiO_2/$MAPbI_3$xClx/Al device structure.[43] Endurance of halide perovskite memristors needs to be further improved to meet the requirements of practical applications. Stability of most halide perovskite memristors is less than 10_3, which is considerably lower than that of other types of memristors. One of the reasons for poor endurance is a lack of understanding in the mechanism behind the switching effect. Improving this understanding will further develop the resistive switching properties of perovskite memristors.

2.2. Perovskite materials

In this section, we will briefly discuss the structural composition of metal halide perovskites, the different dimensions and how this difference influences the electronic-ionic properties of the material.

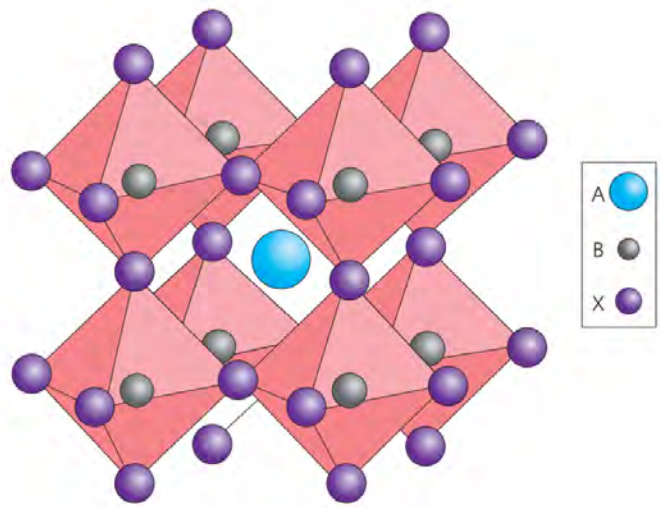

Fig. 2.5: Typical ABX_3 perovskite structure, where A is the monovalant cation and the covalent cation B and monovalent anion halides X together form the octahedral cage. From Reference.[44]

2.2.1. 3D and 2D perovskites

Metal halide perovskites have a crystal structure that share the chemical formula ABX_3, where A is a monovalent cation, and B and X are the bivalent cations and monovalent anions, respectively (see Figure 2.5). The bivalent cations are metals (typically tin Sn^{2+} or lead Pb^{2+}) and form cornersharing BX_6^{4-} octrahedra with the halide anions (chloride Cl^-, bromide Br^-, iodide I^-). The monovalent cation can be either inorganic (cesium Cs^+) or organic (such as methylammonium MA^+, butylammonium BA^+, formamidinium FA^+).[44–46] The variance in composition of halides exhibits a wide range of tunability of the bandgap of the photoactive material, making metal halide perovskites very interesting for application in solar cells and light emmiting diodes.[47,48] The number of octrahedral layers stacked together in the perovskite determines if the structure is 3-dimensional or 2-dimensional. In 2D perovskites, some or all of the A cations are replaced by bulkier organic spacer molecules, which seperate the octrehadral cages. Decreasing the number of octrahedral layers stacked together changes the composition of the chemical formula ABX_3 of the 3D perovskite. For instance, Ruddlesden-Popper 2D perovskites share the formula $(RNH_3)_2A_{n-1}B_nX_{3n+1}$, where RNH_3 is the bulky alky-

lammonium spacer cation, A the monovalent organic cation, B the divalent metal cation and X the halide anion. The number of BX_6^{4-} octrahedra spaced by the alkylammonium spacer cations is represented by the value n.[9,27,49] A fully n=1 2-dimensional perovskite will therefore have the formula $(RNH_3)_2BX_4$, where the BX_6^{4-} octrahedra layers are fully seperated by the bulky organic cation spacers. Figure 2.6 shows the difference in perovskite structure between 3D and 2D perovksites. The insulating organic spacers decrease carrier mobility, which makes 2D perovskites less conductive. The decrease in dimensionality of the perovskite layer increases the energy gap between the conductance and the valance band, as an example from $E_g \approx 1.54$ eV for methylammonium lead iodide ($MAPbI_3$) to $E_g \approx 2.57$ eV for the n = 1 2D perovskite phenethylammonium lead iodide (PEA_2PbI_4).[19]

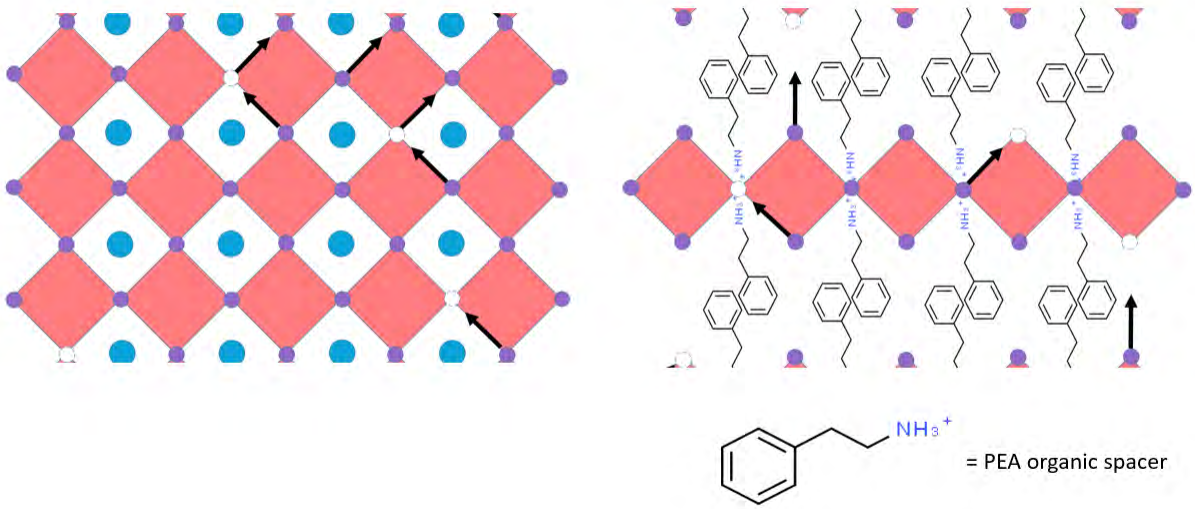

Fig. 2.6: a) Schematic showing the structure of a 3D perovskite, where the arrows show the migration pathways of halides between the conductive octrahedral layers. b) Schematic of n=1 2D perovskite structure, showing the suppression of halide migration due to the presence of large organic cations between the octahedral layers.

2.2.2. Ion migration

The weak chemical bonds between the A cations and the BX_6^{4-} octahedra make structural defects like vacancies and interstitials of the ions within the perovskite lattice easy to form. Depending on low activation energy (E_A) and high mobility, ions can migrate throughout the material, resulting in Current-Voltage (IV) hysteresis.[45] Within the soft crystal lattice of the perovsktite, charged ions migrate upon an external applied voltage bias due their low migration E_A. Taking $MAPbI_3$ as an example, ions migrate due to the presence of vacan-

cies, interstitials or antisite substitutions. Activation energies vary between the ionic species, where there is a wide range of reported E_A values; 0.08-0.58 eV for I^-, 0.46-1.12 eV for MA^+ and 0.80–2.31 eV for Pb^{2+}.[50–53] Among all ionic species, I-ions along the edge of a PbI_6^4 octahedron have the lowest E_A, which is attributed to the shortest migration distance and the lowest electrostatic potential to overcome.[50,54] Ion migration is the fastest and most prominent along surface and grain boundaries, because these present more defects and exhibit lower activation energies for ion migration compared to the bulk.[45,55–58] Solution-processed $MAPbI_3$ thin films have much smaller grains compared to single crystals, raising the defect density within the polycrystalline film.[59] A result of ion migration is a mixed electronic-ionic behaviour where both ions and electric charge carriers can conduct electricity. The organic spacer cations in 2D perovksites can efficiently block ion migration channels.[60] Figure 2.6 also shows a schematic of the 3D and 2D (n=1) perovskite structures and how the presence of large organic cations suppresses the halide movement through the material. The charge and ion mobility is anisotropic, therefore also influencing the conductive channels through the perovskite structure.[27] In short, overall ion migration and carrier mobility is suppressed by the organic spacers that separate the octrahedral layers, which results in a difference in ionic-electronic transport in 3D and 2D perovskites.

2.3. 2D/3D Perovskite Artificial Synapses

The major experimental challenge regarding ion migration in perovksite memristors is to control the type of ions migrating, the concentration of mobile ions and the mobility pathways of ionic species. The exact mechanism behind IV hysteresis and memristive behaviour in perovskites is still unclear. There are different effects that influence the migration of ions, such grain sizes, difference in structured cations and anions, thickness and morphology of the thin film, choice of electrodes and interfaces and magnitude of the applied electric field.[16,23,45,55–57,61] Also, ion migration and hysteresis heavily depends on the scan-rate of the IV sweep. Hysteresis could be minimized with very high and very low scan-rates.[56,57] Another effect that results in IV hysteresis is reactions between the metal electrode and the charged mobile ions in the perovskite material.[22,62,63] The addition of charge transport layers and the different 2D and 3D perovskite layers have a large effect on the resistive switching effect. Having a grasp of the origin of the hysteresis in perovskite memristors is important to understand the mechanisms of how the current flows through the device. This section will clarify how the different mechanisms of interfacial doping and conductive filament formation from Section 2.1.2 might be taking place in different perovskite structures due to ionic diffusion. We will highlight these effects from past research in halide perovskite memristors and mention the debate about the origin of the memristive effect in different 2D and 3D perovskite structures.

2.3.1. Interfacial (doping) effects

The interfacial doping mechanism in perovskites comes forth from the concept of the formation of areas with different conductivities connected in series. In forward bias ($V_{app} > 0$), the generated electric field 'pushes' positively charged cations (A^+) and anion vacancies (V_X^+) with low E_A to the electrode of opposite charge sign. Negatively charged anions (X^-) and cation vacancies (V_A^-) migrate to the positively charged electrode.[56,64] The redistribution of ions and defects at the interface change the electronic effects of the semiconducting material by changing the depletion region and the current flowing through it. The increase of ion density at the electrode interface leads to a linear change in charge-carrier injection barrier.[65] Figure 2.7 shows the band diagram of a p-i-n structure after poling. The charge injection barrier at the electrodes will be smaller due to the formation of the p-i-n structure, therefore increasing the current flowing through the device. This shift in Fermi level will give rise to the memristive effect. As there is debate on the intrinsic carrier concentration in perovskite devices, the formation of the p-i-n structure is an approximation of the effect of ion migration upon an electric field. Under negative bias ($V_{app} < 0$), the polarity of the electrodes switches and will flip the electric

field, therefore gradually moving the charged ions in the opposite direction through the perovksite structure. The dark current density increases upon reversed bias, which indicates that the polarity of the device has been switched to n-i-p polarity, because a negative bias works as forward bias for n-i-p polarity.[56,64,65] The gradual shift of the interface between the differently doped regions results in a gradual switching between conductive states, which corresponds to the explanation of interfacial doping in memristors in Section 2.1.2.

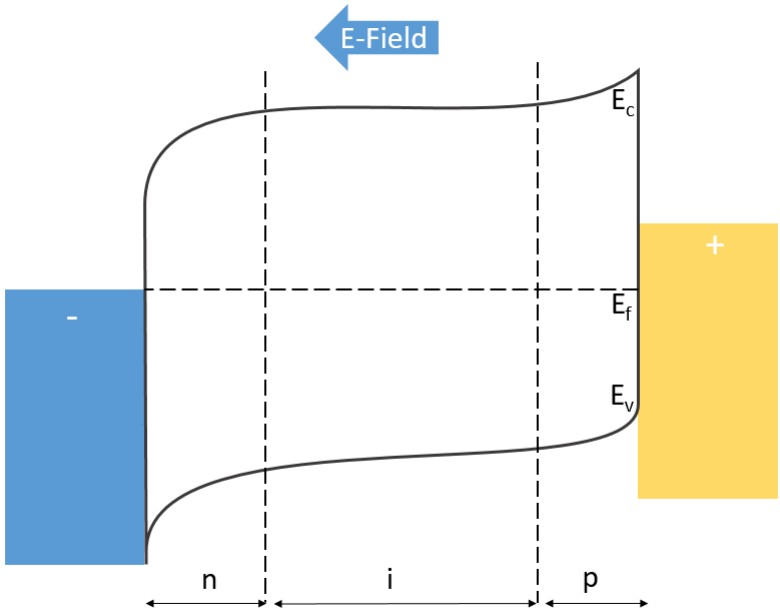

Fig. 2.7: Schematic of n-i-p formation in the perovsite layer, where positively charged ions migrate to the anode, resulting in n-doping, and negatively charged ions migrate to the cathode, resulting in p-doping. Reproduced from Reference.[64] E_v = valance band, E_f = fermi energy, E_c = conduction band.

Research that further elaborates on interfacial effects between the perovskite and electrode is highlighted in methylammonium lead bromide ($MAPbBr_3$) 3D perovskite devices.[66] Figure 2.8 shows a schematic of the possible effect for a n-type perovskite semiconductor. For simplicity, only negatively charged ions are highlighted to explain the effect. Without an external applied bias (A) the bands of the perovskite allign with the electrode to form a Shottky barrier, where electrons will transfer into the metal, resulting in the formation of a depletion region. When a negative bias is applied (B), the initial current through the junction increases rapidly because the bias is in forward bias condition, which easily lets charges flow through the junction. The raising electric field forces the negatively charged ions to migrate to the interface (C), making the perovskite layer at the interface more p-doped, which raises the Shottky barrier height. This decreases the current that can flow through the junction, therefore induces the hysteresis effect in the IV characteristic. Under positive bias

(D), the current remains low due to the junction working as a Schottky diode in reversed bias. Until a high enough electric field allows positive ions to migrate away from the junction, therefore lowering the current even further, resulting in a gradual switching between different resistive states.[66]

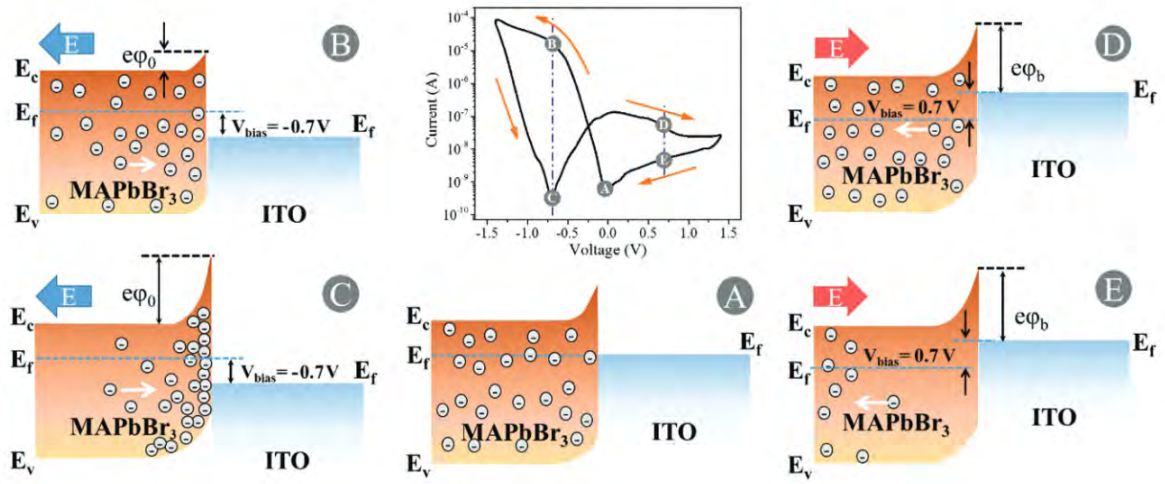

Fig. 2.8: Schematic of ion migration influencing the band alignment at the perovskite/electrode interface, in this case $MAPb_3$/ITO. A shows the intrinsic band alignment without an externally applied voltage bias. B and C show the processes on a negative bias. D and E show the processes in positive bias. The different interfacial stages are highlighted within the measured IV curve in the middle. Figure taken from.[66]

Similar switching mechanisms have been reported in different 2D perovskites with $(PEA)_2Pb_{n-1}MA_nI_{3n+1}$ structures. Hysteresis is suppressed for lower n-values due to the suppression of ion migration in organic spacers.[22] The increase in concentration of insulating PEA cations hinders the conductive pathways of ions along the octrahedral cages, which results in less charge injection into the perovskite structure. Due to less interfacial effects at the interface with the electrode and a lower mobile charge density in the 2D perovksite, both the electronic and ionic transport decreases. Due to the lack of a metallic filament formation in the device, in combination with impedance spectroscopy measurements, the activation process of conductive switching is due to physical and chemical reactions at the interface.

2.3.2. Conductive filament formation

The conductive filament formation in perovskites comes forth from the concept of the rearrangement of ions or ionic vacancies between the electrodes, which drastically changes conductivity when formed. This mechanism is activated either by positively charged ion vacancies V_A^+ or metallic silver (Ag) ions that actively distribute through the layer of the device.[67,68] In fully 2D n=1 PEA_2PbBr_4 single crystal exfoliated flakes, drastic changes in conductance were measured and local elemental distribution through the device was studied with cross-sectional scanning transmission electron microscopy (STEM) and energy-dispersive X-ray spectroscopy (EDS). In the bulk, the Br^- ions were initially uniformly distributed, while they accumulate at the gold interface after a voltage bias. Br^--ions are therefore able to efficiently hop inbetween the insulating organic cation spacers. This shows that signifiacant ion migration is apparent in n=1 2D perovskites. As the Br^- ions migrate out of the bulk crystal of the perovskite, the remaining V_{Br}^+ vacancies form a conductive filament of around 20 nm in diameter. Figure 2.9 shows a schematic of the effect in these single crystal devices.[27]

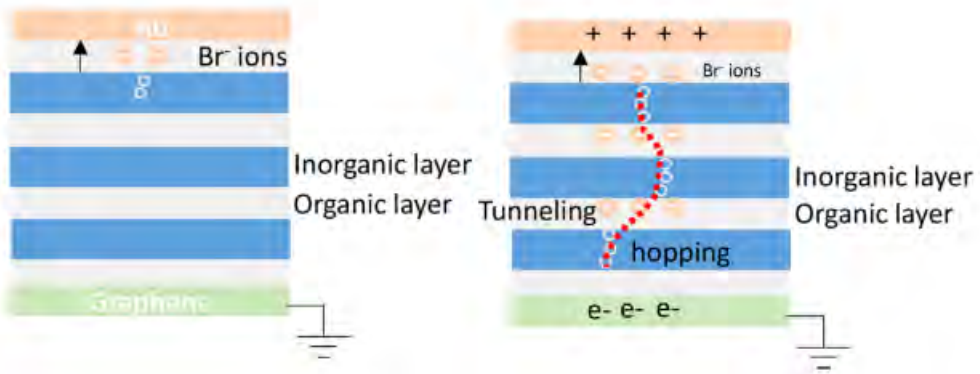

Fig. 2.9: Schematic of ion migration promoting a conductive filament formation of Br^- vacancies in single crystal 2D n=1 PEA_2PbBr_4 perovskites. Figure taken from.[27]

Filament formation in 3D perovskite devices has also been observed for $MAPbI_3$, where IV measurements were performed in combination with conductive atomic force microscopy (c-AFM) to measure the conductivity of the active surface of the perovskite thin film. In order to perform these measurements, devices were poled to the ON state, after which the top electrode was accurately scraped off with the diamond tip of the AFM probe. After this, the conductance of the surface of the perovskite was locally measured by applying a read voltage of 15 mV on a 175 by 175 nm scan area. With c-AFM measurements, a high conductive area of 50 nm on the surface of the perovskite layer was observed, which gives rise to the formation of a filament of iodide vacancies in the device.[69] In contrast to gradual changes in conductivity due to interfacial effects, the

formation of conductive filaments results in abrupt changes in conductivity.[70]

2.3.3. Device structure in this research

In this research, we attempt to understand the difference in memristive switching effects in 2D and 3D perovskites. We perform a comparison study between the 3D perovskite $MAPbI_3$ and the 2D perovskite PEA_2PbI_4 thin film devices. To measure the difference in memristive properties between 3D and 2D perovskite thin films, we first establish the different materials used in this research and how these influence the device measurements. The configurations of the devices used in this thesis will be explained paired with the corresponding band diagram, portrayed in Figure 2.10. The active perovskite layers $MAPbI_3$ and PEA_2PbI_4 are compared within a hole-transport layer structure. Starting from the bottom, indium tin oxide (ITO) serves as a transparent conducting bottom contact. On top of the ITO, a organic hole transport layer PTAA (hole mobility is 7.47 x 10^{-5} $cm^2V^{-1}s^{-1}$) is deposited.[71] The solution-processed $MAPbI_3$ and PEA_2PbI_4 thin films serve as the active layers in the device. Further investigation of the memristive effect is investigated by addition of another organic hole transport layer Spiro-OMeTAD (hole mobility is 2 x 10^{-4} $cm^2V^{-1}s^{-1}$) is deposited on top of the perovskite layer.[71] As a top contact, gold (Au) is deposited to finish the device configurations. As this is a hole-only device, we only expect hole current to flow through it.[72]

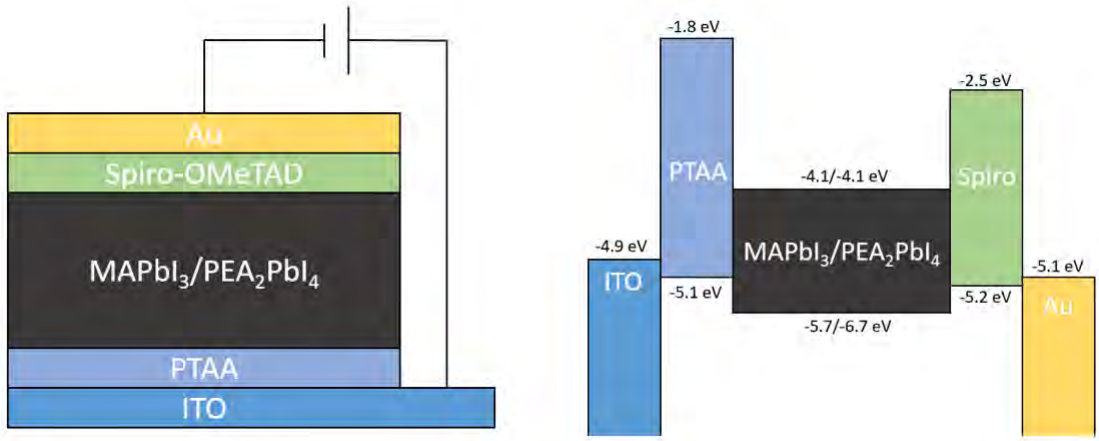

Fig. 2.10: left: A schematic overview of the device configurations. right: A schematic overview of the band diagram of the different semiconducting materials.[19,71,73,74]

We fabricate devices with four different configurations in this research, where we keep the electrodes and the bottom transport layers constant. This results in the investigated devices $MAPbI_3$, $MAPbI_3$/Spiro, PEA_2PbI_4 and PEA_2PbI_4/Spiro. On these devices, we perform IV measurements to investigate the influence of the combination of perovskite and transport layers on the switching effect. The parameters we focus on in

analyzing this difference is the operating current, the magnitude of the ON/OFF ratio and the stability of the device upon multiple subsequent voltage stresses. Due to the presence of the large organic spacers, we expect the 2D perovskite PEA_2PbI_4 to be less conductive and show a reduction in switching effect. By addition of the Spiro-OMeTAD transport layer, we expect lower overall conductivity due to the hole-only device structure. Also, we expect the Spiro-OMeTAD layer to block chemical reactions between the perovskite and top gold electrode.

3. Methodology

3.1. Preparation of thin films

In this section, the different fabrication methods of the active layers of the device are explained in chronological order from the bottom of the device to the top contact layer. After the annealing step of each spincoated thin film, the substrate was left to cool down to room temperature before the subsequent layer of the device stack was deposited. All thin films were deposited in a nitrogen filled glovebox (O2 < 5.0 ppm), unless stated otherwise. For the fabrication method, the following chemicals were used: Dimethyl sulfoxide (DMSO, anhydrous 99.9%), toluene, chlorobenze, dimethylformamide (DMF), phenethylammonium iodide (PEAI, 99.999%) and poly(triayl-amine) semiconductor (PTAA) were purchased from Sigma Aldrich. Methylammonium iodide (MAI) was purchased from Solaronix, lead iodide (PbI_2, 99.999%) was purchased from TCI. All chemicals were used without further purification. Samples were prepared on ITO coated glass substrates.

3.1.1. Cleaning ITO coated substrates

15 by 15 mm Indium Tin Oxide (ITO) coated glass substrates were used as a transparent bottom contact. The substrates were cleaned with a brush using liquid detergent before sequentially sonicating them in an ultrasonic bath for 20 minutes in demineralised water, acetone, and isopropanol. To further remove impurities and contaminants from the surface and increase the wettability of the active surface, the substrates were exposed to oxygen plasma for 16 minutes at an oxygen flow of 0.2 standard cubic centimetres per minute (sccm), with a power of 100W.

3.1.2. PTAA bottom transport layer

PTAA precursor solution was prepared by dissolving PTAA (2 mg) in toluene (1.000 mL) and stirring overnight at 500 rpm at 30 °C. 75 μL of PTAA precursor solution was spincoated onto the substrate at 5000 rpm for 35 seconds. Immediately after the spincoating process, the samples were annealled at 100 °C for 10 minutes.

3.1.3. Perovskite thin film

MAI (235.0 mg) and PbI_2 (681.5 mg) were dissolved in DMSO (0.095 mL) and DMF (1.000 mL) by stirring overnight at 400 rpm at 30 °C. 80 μL of the precursor solution was spincoated on the substrate at 4000 rpm for 30 seconds. Immediately after the spincoating process, the samples were annealled at 100 °C for 10 minutes.

PEAI (242.4 mg) and PbI_2 (220.2 mg) were dissolved in DMF (1.000 mL) by stirring overnight at 400 rpm at 30 °C. 80 μL of the precursor solution was spincoated onto the substrate at 4000 rpm for 30 seconds. The samples were afterwards annealled for 15 minutes at 75 °C.

3.1.4. Spiro-OMeTAD top transport layer

The Spiro-OMeTAD precursor solution was prepared by dissolving Spiro-OMeTAD (10 mg) in chlorobenzene (1 mL) and stirring overnight at 500 rpm at 30 °C. 50 μL of Spiro-OMeTAD precursor solution was spincoated onto the substrate at 4000 rpm for 30 seconds with an acceleration of 800 rpm/s. The samples were not annealed after this process.

3.1.5. Au top contact layer

To complete the device, gold (Drijfhout, 99.99 %) was deposited by thermal evaporation. An Amod physical vapor deposition system from Ångstrom, mounted inside a nitrogen-filled glovebox, was used under a high vacuum (5×10^{-7} to 10^{-8} torr). The vacuum accurately controls the rate of vaporized material that travels to the target substrate, where they condense back to a solid state. Gold was deposited at 0.01 nm/s for the first 10 nm and afterwards with a rate of 0.1 nm/s up to a final film thickness of 100 nm.

3.2. Characterization

3.2.1. Material Characterization

X-ray diffraction (XRD) patterns of the fabricated perovskite thin films were obtained to identify the crystal phase by measuring the diffracted X-rays from the sample under a variable angle θ. A Brucker D2 diffractometer, using the Bragg-Brentano configuration with Cu-Kα (= 1.54 Å) radiation, measured a range set from 5.0° to 50.0°, with an 0.02° increment step and a dwell time of 0.1 seconds.

The thickness of the thin films were measured by scratching away the surface of the film and using a KLA Tencor Stylus profiler P7 profilometer, where a calibrated needle moved along the surface to measure the height difference between the trench and the film. Measurements were acquired by applying a force of 0.5 - 2 mg and measuring at a speed of 20 µm/s, while recording at 200 Hz.

Further film thickness and surface morphology were characterized with Atomic Force Microscopy (AFM). Measurements were done with a Bruker Dimension Icon-PT Atomic Force Microscope, using the PeakForce

mode of operation and a ScanAsyst Air probe. Images were acquired with a scan size of 1x1 μm, a scan rate of 0.200 Hz and 512 samples/line.

Scanning Electron Microscopy (SEM) measurements were obtained with a FEI Verios 460 scanning electron microscope. Under a high vacuum, an electron beam travels through electromagnetic fields and lenses, which focus the electron beam on the sample. The scattered electrons from the sample are collected to form a final image. Heavy atoms backscatter the electronbeam more efficiently than elements with lower mass, which gives rise to distinction of contrast in the electron image. In this research, SEM images were taken to measure both the surface morphology of the perovskite films and cross-sections of the the device stack. Images were acquired with a beam voltage of 5kV and a current of 100 pA.

3.2.2. Device Characterization

Current-Voltage (IV) curves were measured with a Keithley 2440 5A Source/Measure Unit (SMU) to oversee the current characteristics of the fabricated devices upon a increasing and decreasing voltage sweep. IV measurements were executed by starting from -1V to +1 V and back from +1V to -1V. The amplitude of the voltage sweep was increased until a noticable hysteresis was detected. The IV sweep was then repeated a total of 5 times to show the reproducibility of the hysteresis effect. The measurements were performed with a rate of 0.1V/s. The current compliance or limit was set at 50 mA as a safety feature to prevent a high current from flowing through the device and therefore irreversibly breaking the functional layers.

Voltage pulse measurements or Pulsed Voltage Stresses (PVS) were obtained with an Agilent B2902A Precision SMU to measure the output current of the device upon subsequent pulsed voltages stresses. These experiments were conducted to investigate the shortest pulse time needed for a change in conductivity/switching event. Also, these measurements will give accurate information on the power consumption needed for a switching event. The measurements were performed with voltages between -1V and 1V, and with a pulse duration between 480 ms and 8 ms. The current compliance was set at 5mA.

4. Results and Discussion

In this chapter, the results of the measurements are presented and the main observations and differences in $MAPbI_3$ and PEA_2PbI_4 device stacks are discussed. In the first part of this section, the comparison between the perovskite materials are stated in terms of crystal structure, morphology and thickness. Then, we present IV sweeps of the devices to measure the hysteresis and operating current upon a voltage bias. As a follow up, endurance of devices is measured by subsequently performing IV sweeps until a 'break point', where there is no hysteresis measured. Afterwards, the effect of the addition of a Spiro-OMeTAD (Spiro) transport layer within these devices stacks are discussed. Lastly, we discuss the results of Pulsed Voltage Stresses (PVS) on the devices, where we present the shortest pulse time, the highest ratio and the lowest energy consumption to induce a switching effect.

4.1. Characterization of thin films

Thickness and morphology of the bottom and top organic transport layers fabricated in this research in Section 3.1.2 and Section 3.1.4 were measured with both profilometer and AFM as explained in 3.2.1. The thickness of the thin films is 10 nm for PTAA and 60 nm for Spiro-OMeTAD. The measurements showed no pinholes and a overall smooth surface. Further information on the material characterization of these transport layers in the device stack is highlighted in the Appendix Section 8.1 and Section 8.2. Following the perovskite thin film fabrication procedure from Section 3.1.3, the crystal phase of the $MAPbI_3$ and PEA_2PbI_4 perovskite thin films was measured with XRD. Figure 4.1 shows distinctive (110) and (220) relative intensity peaks for $MAPbI_3$ at 14.0° and 28.0° and (002), (004), (006), (008), (0010), and (0012) peaks for PEA_2PbI_4 from 5.5° to 27.5°, which corresponds to the patterns in literature.[75,76] The intensity and confinement of the peaks show that the fabrication method of the thin films has allowed the perovskite film to sufficiently grow into cubic crystal phase.

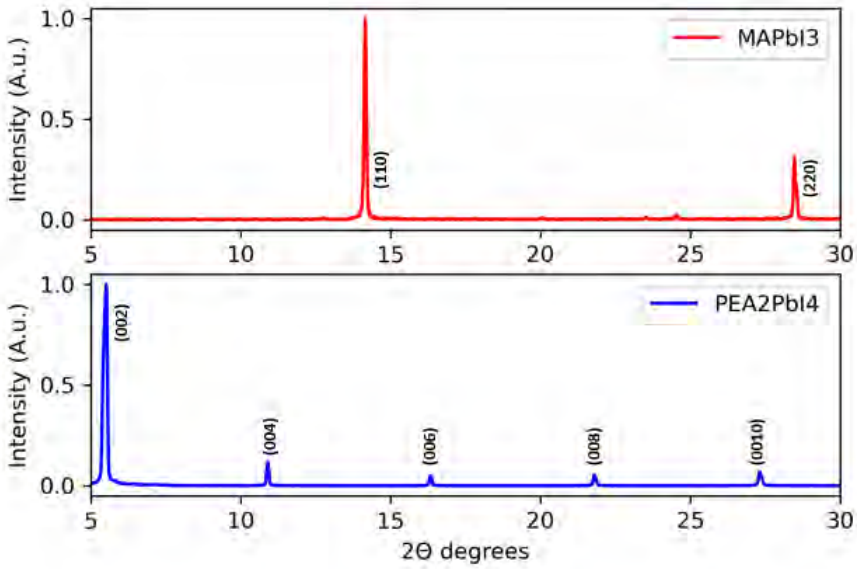

Fig. 4.1: XRD spectra of the $MAPbI_3$ and PEA_2PbI_4 perovskite thin films.

Figure 4.2a shows a top view SEM image of the surface of the $MAPbI_3$ thin film, clearly showing typical small polycrystalline grains of a solution-based perovskite thin film.[59] The PEA_2PbI_4 thin films were more difficult to image with SEM (Figure 4.2b). Imaging of the PEA_2PbI_4 samples with SEM was difficult because of charging effects. AFM images of the surface of both films were acquired to present a better comparison of their morphology with high resolution.

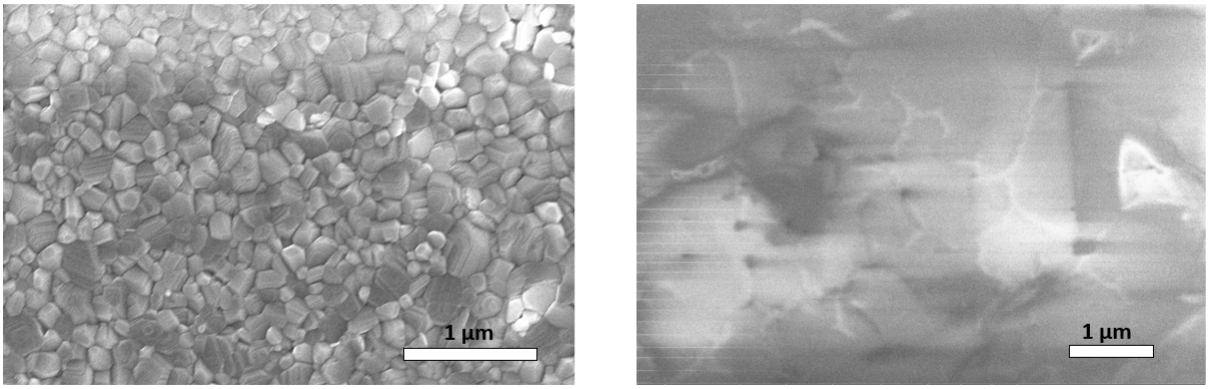

Fig. 4.2: a) Top SEM image of the $MAPbI_3$ thin film. b) Top SEM image of the PEA_2PbI_4 thin film.

AFM measurements were conducted following the procedure in Section 3.2.1 to compare the grain sizes and morphology of the $MAPbI_3$ and PEA_2PbI_4 thin films. Again, differences in features are easy to distinguish for $MAPbI_3$. In Figure 4.3a, $MAPbI_3$ grains are estimated to vary between 50-300 nm. In Figure 4.3b, PEA_2PbI_4 thin film grainsize features are again difficult to distinguish. However, the AFM image shows features that may be indicated as grains. There is too much overlap between the features to give a good estimation on grain sizes. As reported, AFM and SEM measurements are ambiguous techniques to accurately determine grainsize and crystal orientations in perovskites.[77] Further research is needed to precisely compare the grain sizes of $MAPbI_3$ and PEA_2PbI_4 thin films. Since ion migration is significantly increased along grain boundaries, it is important to take the incomplete information on grain size comparison into consideration in further measurements.[58] The calculated Root Mean Square (RMS) roughness of the $MAPbI_3$ thin film is 7.8 nm, compared to 1.9 nm for PEA_2PbI_4, which further demonstrates smooth perovskite film fabrication.

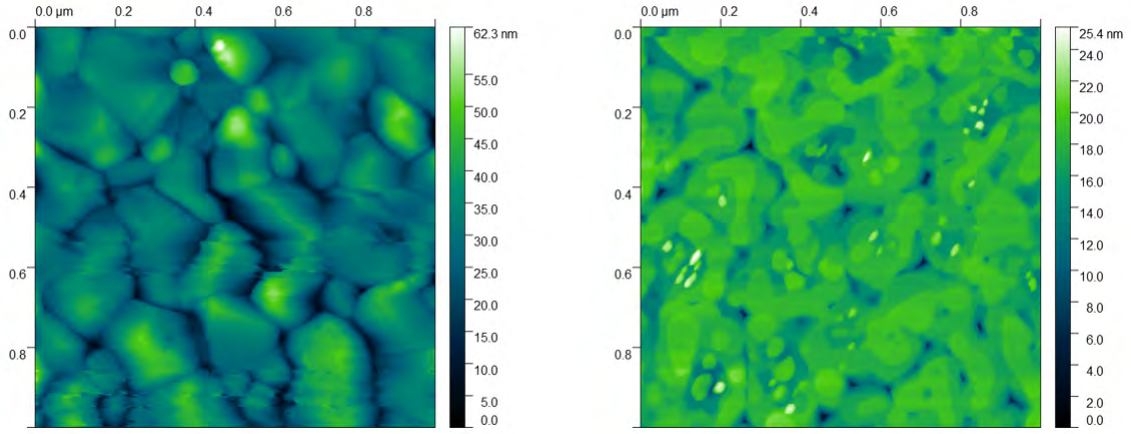

Fig. 4.3: a) 1x1 μm top AFM image of the $MAPbI_3$ thin film. RMS roughness is 7.763 nm. 1x1 μm top AFM image of the PEA_2PbI_4 thin film. RMS roughness is 1.938 nm.

Figure 4.4a shows the cross-sectional SEM image acquired of an ITO/PTAA/$MAPbI_3$/Au device. The determined thickness of the $MAPbI_3$ thin film is 500 nm ± 50nm. Figure 4.4b shows the cross-sectional SEM image acquired of an ITO/PTAA/PEA_2PbI_4/Au device. In this image, we determine a thickness of the PEA_2PbI_4 thin film of 400 nm ± 50nm. For both cross-sectional images, a smooth perovskite surface is observed. The fabrication method in Section 3.1.3 results in a comparable thickness of the perovskite thin films. Since thin films activate a switching behaviour at lower potential values, characterizing the difference is essential to compare the operations of these devices.

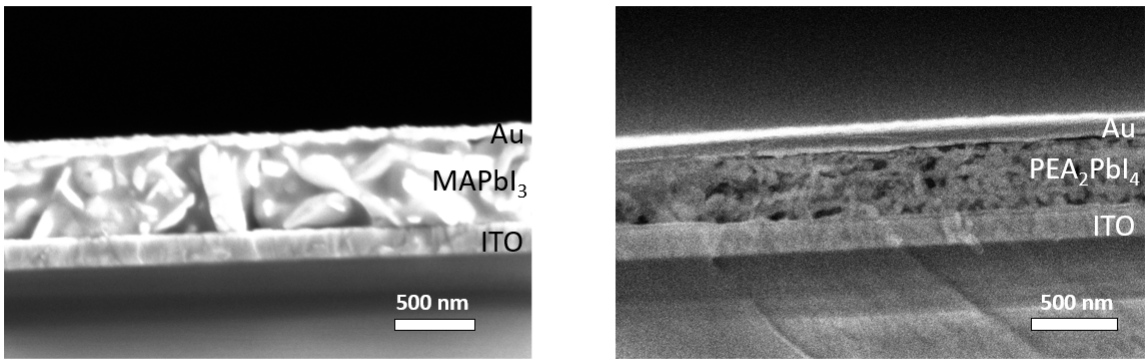

Fig. 4.4: a) Cross-sectional SEM image of an ITO/PTAA/$MAPbI_3$/Au device. b) Cross-sectional SEM image of an ITO/PTAA/PEA_2PbI_4/Au device. The PTAA film is not highlighted in these images as a result of its thin appearance (see Section 8.1).

4.2. 3D VERSUS 2D

Following the experimental methods from Section 3.2.2, we present the results of the $MAPbI_3$ and the PEA_2PbI_4 memristive devices by comparing their IV curves and endurance upon multiple cycles.

4.2.1. IV CURVES

Figure 4.5a presents the typical IV-characteristics for the $MAPbI_3$ device under 5 subsequent DC voltage sweeps between -1V and +1V. The absolute measured current is presented on the logarithmic scale. The current flowing through the device is initially low (10^{-6}-10^{-5} A) until around +0.7V, where the current drastically increases to 10^{-3} A at +1V. Sweeping back to lower voltages the conductivity stays high, which means the device is in the ON state. Between +0.20V and -0.25V, the measured current is negative and very low (10^{-8}A-10^{-6}A), until it drastically increases again in the negative applied bias. The device gradually switches back to the less conductive state (OFF state) in the negative bias, where the initial measured current through the device is similar again in the positive bias.

Figure 4.5b shows the first curve of 5 subsequent IV sweeps for the PEA_2PbI_4 perovskite device between -1.5V and +1.5V. Here, we only show the first sweep for clarification. Figure 8.4b in the Appendix shows all 5 subsequently measured IV sweeps. This device was also first measured between -1V and +1V, but no hysteresis effect was measured (see Figure 8.4a in the Appendix). Initially. the current flowing through the device is < 10^{-7}A. Around +1V, there is some stochastic switching in conductivity, until the device switches to the ON state, where measured current is around 10^{-6}A. In the negative applied bias, a similar behaviour is presented, but the ratio between the two conductive states is lower and less profound.

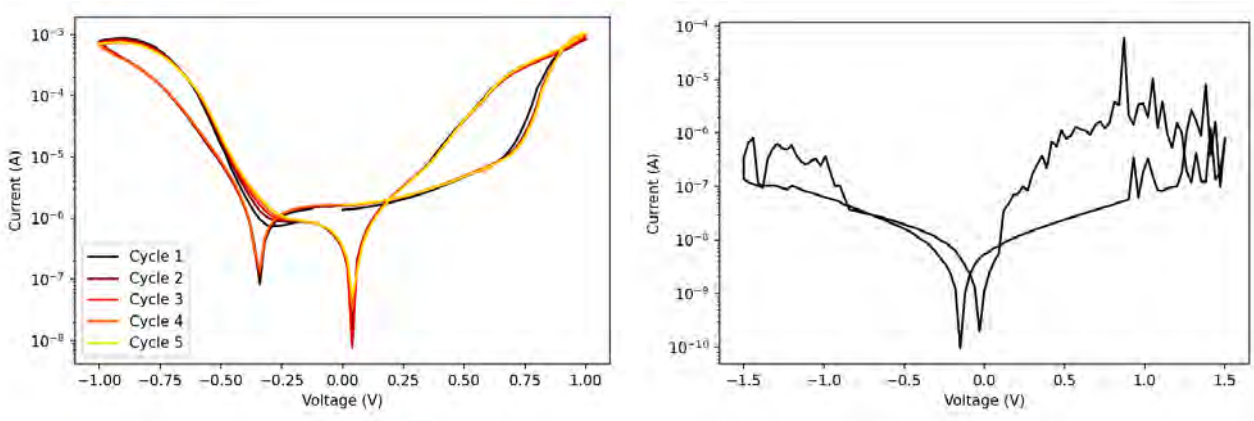

Fig. 4.5: a) 5 subsequent IV characteristics of the $MAPbI_3$ device. b) First IV sweep of 5 subsequent sweeps in PEA_2PbI_4 device from Figure 8.4b.

From these results, we can observe the difference in both the operating current and hysteretic switching effects between these devices. Looking at the operating current, the OFF state is reduced by at least 1 order of magnitude for the PEA_2PbI_4 ($< 10^{-7}$A) compared to $MAPbI_3$ (10^{-6}A). Also in the ON state, the measured currents are lower, which corresponds to the hypothesis of less current output due to decrease of carrier mobility and anisotropic charge transport in 2D perovskites.[19,27] Looking at the operation of the hysteretic effects in both devices, we observe that the initial behaviour of the $MAPbI_3$ device is very diode-like, where at +0.7V the current flowing through the device rapidly increases to higher conductivity. In the reversed IV scan, the current is higher, which follows the hypothesis of interfacial doping or other interfacial effects that at the electrode interface.[66] Another interesting observation in the $MAPbI_3$ device is that the current is not 0A at 0V bias. A reason for this could be a charging effect due to ions still migrating through the device. The IV behaviour of the PEA_2PbI_4 device is not diode-like, but does show a significant hysteretic switching behaviour at higher voltage ranges. This observation is interesting, because of the reported blocking of ion migration channels by the large organic spacers in 2D perovskites.[60] In Figure 8.4b, stochastic switching at different voltages is observed, hindering a reproducible behaviour over multiple cycles. However, from these IV sweeps we can conclude that there is efficient ionic transport and low observed current in PEA_2PbI_4 perovskite devices to induce a resistive switching effect.

4.2.2. Endurance measurements

Endurance of devices was measured by performing multiple subsequent IV sweeps according to the methods in Section 3.2.2 over the perovskite devices. The endurance is analyzed by calculating the difference in high conductive ON values and low conductive OFF values. These values were calculated by dividing the ON current by the OFF current at a certain voltage value V_{read}, where a subsequent high hysteresis is measured. For the $MAPbI_3$ device, the devices were poled between -1V and +1V. The large observed switching was in the reverse bias, therefore the V_{read} was set at -0.5V. The PEA_2PbI_4 devices were poled between -2V and +2V. The V_{read} was set at +0.5V, because in the forward bias over multiple sweeps significant switching was detected. Figure 8.6 in the Appendix portrays all the subsequently measured IV curves and the set values for V_{read}. The results are presented in Figure 4.6, which shows a scatter plot of the high conductive ON values and low conductive OFF values over multiple cycles.

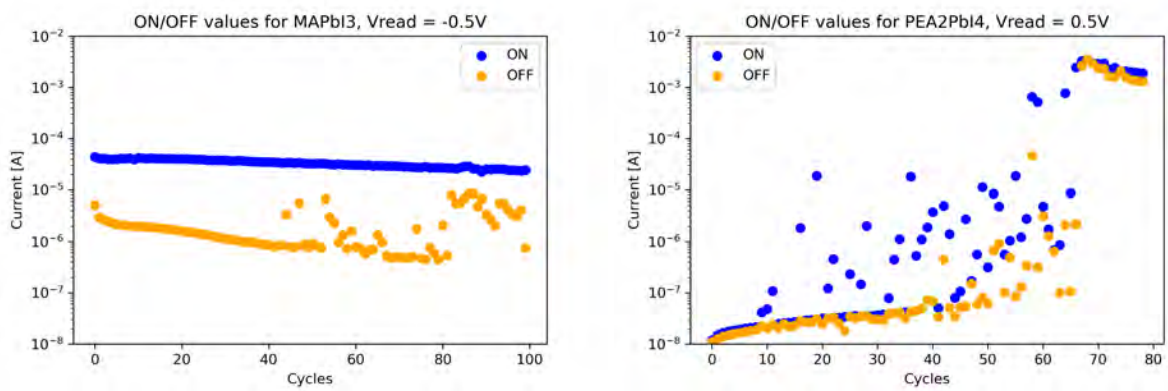

Fig. 4.6: a) Evolution of the ON and OFF values of the $MAPbI_3$ device, V_{read} = -0.5V. b) Evolution of the ON and OFF values of the PEA_2PbI_4 device, V_{read} = +0.5V.

In Figure 4.6a, the ON and OFF currents of the $MAPbI_3$ device are initiallly $4x10^{-5}$ A and $5x10^{-6}$ A, respectively. The progression of the ON state is consistent over the endurance measurement, where OFF state gradually loses its conductivity to $1x10^{-6}$ A after 40 cycles. After 45-50 cycles, the device starts to lose its memristive effect, where incidental higher conductive OFF states are observed. After 80 cycles, the device degrades by irreversibly losing a well-defined difference in the ON and OFF states. From here, the device has lost its resistive switching effect. In Figure 4.6b, the measured difference in ON and OFF current values for PEA_2PbI_4 is again stochastic. For the first 10 cycles, the operating current at V_{read} is on the order of 10^{-8} A for both the ON and OFF stte. This means that there is no distinct switching measured between high and low conductive states. Between cycle 10 and cycle 70, the OFF state gradually increases in conductivity, and stochastic ON currents are measured. For some cycles, the observed ON/OFF ratio is in the 10^{-3} range. After

70 cycles, the device short circuits and loses its memristive effect.

From these endurance measurements, we can further argue that $MAPbI_3$ devices show reproducible switching behaviour of 1 order of magnitude over multiple cycles. The 'breaking point' of the memristive operation of the device is around 80 cycles. Reasons for this could be the increased amount of defects in the perovskite material due to subsequent migration of ions, or irreversible chemical reactions with the gold electrode and the iodide ions.[62] The switching effect of the PEA_2PbI_4 devices is very inconsistent, where on numerous cycles there is no detected difference between the ON and OFF state. At the 'breaking point' at 70 cycles, the device short circuits to high currents. These results further imply the unreliable memristive effect of 2D perovskites.

4.3. Addition of Spiro-OMeTAD transport layer

In this section, we present the results on the IV curves and endurance measurements for the addition of a Spiro-OMeTAD thin film to the device (see Section 3.1.4 for the fabrication process). Note that the Spiro thin film was added on top of the perovskite structure, resulting in the full device architecture from Figure 2.10a.

4.3.1. IV curves

Figure 4.7a presents the IV curves for the $MAPbI_3$/Spiro device under 5 subsequent DC voltage sweeps between -2V and +2V. We observe an abrupt ON switching at 1.7V in the 2nd and 4th cycle, and within the same cycle an abrupt OFF switching at -2V. The calculated ON/OFF ratio within these cycles is more than 2 orders of magnitude. After multiple measurements we were unable to reproduce this switching effect. The IV curves of PEA_2PbI_4/Spiro in Figure 4.7b show ON switching in the positive bias. This happens at different voltage magnitudes. The device switches OFF in the negative bias at low voltages, between 0V and -0.5V.

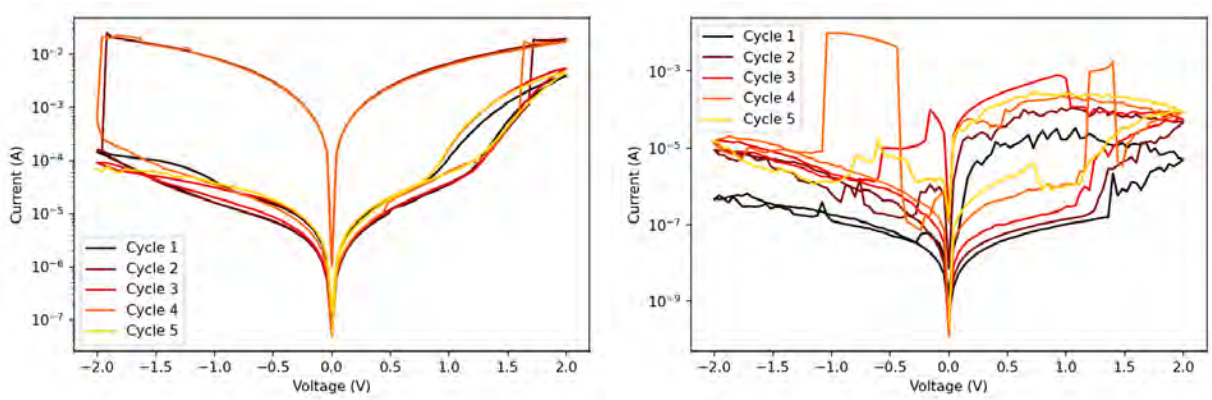

Fig. 4.7: a) IV curves of $MAPbI_3$/Spiro and b) PEA_2PbI_4/Spiro devices under 5 subsequent DC voltage sweeps. See Figure 8.5 for more IV sweeps.

Comparing these IV curves to the devices in Figure 4.5, a clear difference can be seen in the conductive switching behaviour. First of all, for the $MAPbI_3$/Spiro device in Figure 4.7a, there is abrupt switching observed, which was never observed for devices $MAPbI_3$ without a Spiro layer. Also at higher voltage biases, the $MAPbI_3$-only devices show gradual switching as portrayed in Figure 8.5a in the Appendix. For some devices, the abrupt switching is observed also at lower voltages and is very stochastic, as can been seen in Figure 8.5b in the Appendix. A reason for the difference in this behaviour could be that a certain voltage potential value, ions migrate from the perovskite into the Spiro layer, which has been reported in previous research.[60] As a consequence, anion vacancies (I^-) that are left in the perovskite layer may form a channel for electrons to efficiently move between the ITO and gold electrode. This effect could promote a lower potential barrier for

conductive filament formation. For PEA_2PbI_4/Spiro devices, we still measure lower currents and see an overall increase of the difference in the ON and OFF states. Because switching is still stochastic, it is, however, unclear if this is due to effects in the Spiro layer or in the pristine perovskite film.

4.3.2. Endurance measurements

Endurance of these devices is again analyzed by measuring the high conductive ON values and low conductive OFF values within every IV sweep. Figure 8.7 in the Appendix portrays all the subsequently measured IV curves and the set values for V_{read} for both the $MAPbI_3$/Spiro and PEA_2PbI_4/Spiro devices. $MAPbI_3$/Spiro devices were poled between -1V and +1V. PEA_2PbI_4/Spiro devices were poled between -1.5V and +1.5V. The results of for both devices are portrayed in Figure 4.8. In Figure 4.8a, the $MAPbI_3$/Spiro device has an OFF state of $5x10^{-7}$ A and an ON state of $4x10^{-6}$ A in the first cycle at V_{read} = 0.5V. During the measured cycles, the ON state becomes more conductive, reaching a current value of $1x10^{-5}$ A after 100 cycles. The OFF state loses its conductivity upon repeated measurements, reaching a current value of $3x10^{-7}$ A after 100 cycles. For PEA_2PbI_4/Spiro (Figure 4.8b), the progression of the ON and OFF states upon multiple cycles is still very stochastic. ranging between 10^{-7} A - 10^{-4} A for the OFF state and 10^{-7} A - 10^{-4} A for the ON state. After 100 cycles, there is still a switching effect measured, which means the device has not degraded.

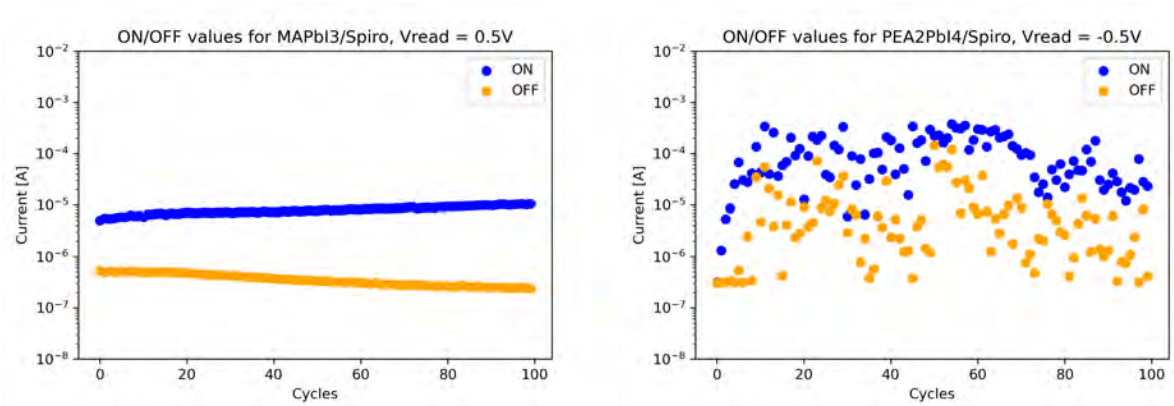

Fig. 4.8: a) Evolution of the ON and OFF values of the $MAPbI_3$/Spiro device, V_{read} = +0.5V. b) Evolution of the ON and OFF values of the PEA_2PbI_4/Spiro device, V_{read} = -0.5V.

From these measurements, there are two interesting observations which we will discuss. Firstly, the devices with a Spiro-OMeTAD film show better endurance compared to the devices in Figure 4.6, both still having their memristive effect after 100 cycles. A reason for this could be that the Spiro film serves as a protection layer that blocks irreversible redox reactions between the gold ions and accumulated halide ions at the top electrode/perovskite interface.[62] Secondly, the addition of the Spiro layer lowers both the ON and

OFF current for $MAPbI_3$ devices by one order of magnitude, from 10^{-4} A and 10^{-5} A to 10^{-5} A and 10^{-6} A, respectively. For PEA_2PbI_4 devices, it is still difficult to see the true difference in ON and OFF currents with and without the Spiro layer, because of the stochastic switching behaviour. For these devices, we will further analyze their memristive behaviour upon multiple cycles by calculating the ON/OFF ratio. This is simply done by dividing the ON current by the OFF current within each cycle. Figure 4.9a shows a scatter plot of the calculated ON/OFF ratios over the subsequent IV cycles of the measured current values portrayed in Figure 4.8. For the $MAPbI_3$ device, the ON/OFF ratio increases over 100 IV sweeps, from 10-50. For PEA_2PbI_4, there is no trend seen in the ON/OFF ratio over 100 cycles. Figure 4.9b presents a histogram distribution of these values, which more clearly shows the distributed ON/OFF ratios of the $MAPbI_3$ and PEA_2PbI_4 devices. These results provide further prove on the difference in switching effects in the $MAPbI_3$ and PEA_2PbI_4 devices. PEA_2PbI_4 devices have potentially a high ON/OFF ratio of $>10^2$, but the distribution shows that these values are reached only incidentally. From these measurements, there is a chance distribution of these ON/OFF values, which further portrays the stochastic switching behaviour of the PEA_2PbI_4 device.

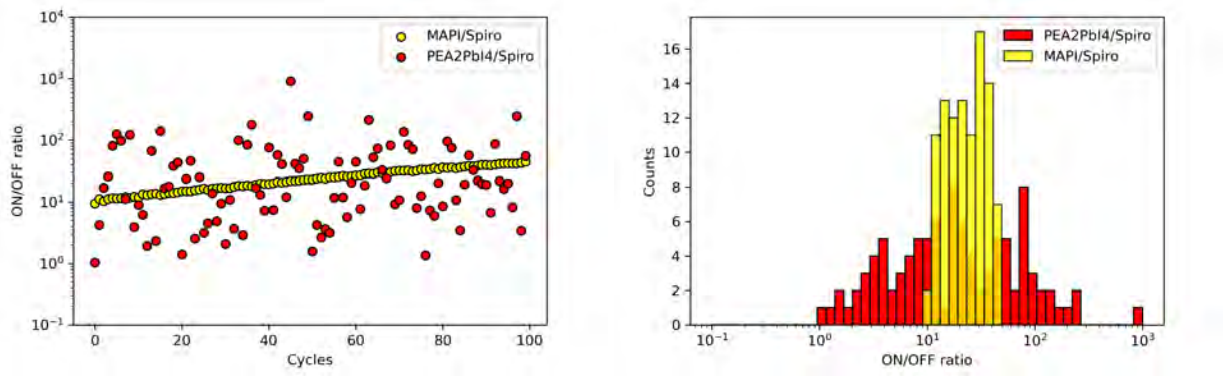

Fig. 4.9: a) Scatter plot of the ON/OFF ratios calculated from the plots in 4.8 for $MAPbI_3$/Spiro (yellow) and PEA_2PbI_4/Spiro (red). b) Histogram of the data plots in 4.8, which shows the occurance of a ON/OFF ratio within the 100 IV sweeps.

From these measurements, we can conclude that we have successfully improved our device performance by addition of a Spiro-OMeTAD transport layer between the perovskite film and the top gold electrode. These improvements are easily observed in $MAPbI_3$ devices by a lower measured current by 1 order of magnitude, higher overall ON/OFF ratio (from 10 to 50) and a longer endurance of >100 cycles to reach a 'breaking point'. For PEA_2PbI_4, there is no positive trend measured in operating current, where the measured ON and OFF currents are higher. Endurance of the device is improved, where higher ON/OFF ratios (1 - 100) are measured and the 'breaking point' is > 100 cycles.

4.4. Pulsed Voltage Stresses

The champion devices with a Spiro-OMeTAD transport layer from Section 4.3 were further analyzed with Pulsed Voltage Stress (PVS) measurements according to the methods explained in section 3.2.2. These measurements will give more insight on triggering the device between OFF and ON state upon short pulse stimulation, analogous to the biological system.[39] Moreover, with introduction of the the short pulse duration in these measurements, energy consumption on changing the conductive state can be calculated with Equation 2.6. The measurements were conducted by first performing an IV sweep on the devices to oversee in which voltage polarity the device has a large switching effect. Figure 4.10a shows that the switching effect for $MAPbI_3$/Spiro is in the positive bias, where Figure 4.10b shows a very abrupt switching effect in the negative bias for PEA_2PbI_4/Spiro.

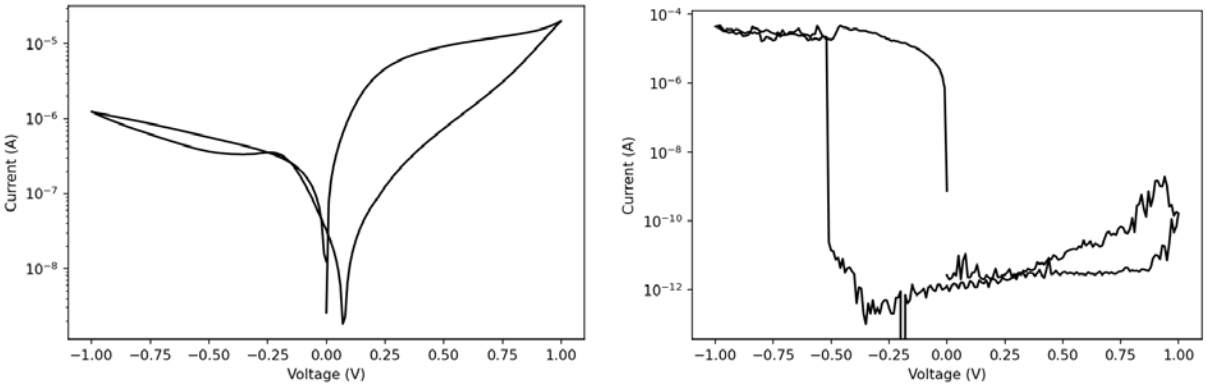

Fig. 4.10: IV sweeps done on the pixels before the pulse measurement.

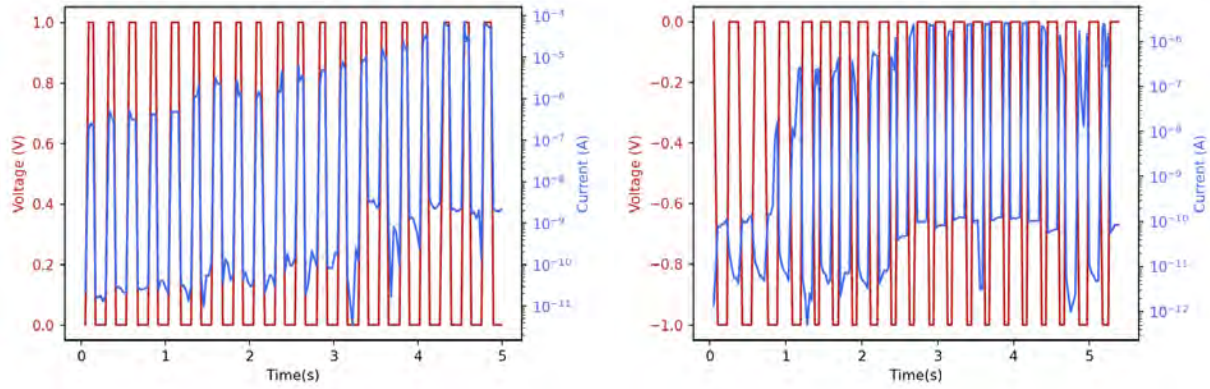

Fig. 4.11: Pulsed Voltage Stress measurements of the $MAPbI_3$/Spiro (left) and PEA_2PbI_4/Spiro (right) devices. Note that for these measurements,

Following the methodology from Section 3.2.2, Figure 4.11a presents that 18 subsequent +1V pulses of 50 ms were needed to switch the conductance of the $MAPbI_3$/Spiro device by 2 orders of magnitude. The current measured at the first voltage pulse was 2×10^{-7} A, and the measured current after switching was 7 x 10^{-5}. This results in an energy consumption per pulse ranging from 1×10^{-8}J to 3×10^{-6}J (10 nJ to 3μJ). In Figure 4.11b, we observe that 12 subsequent -1V pulses of 120 ms were needed to switch the conductance of the PEA_2PbI_4/Spiro device by 4 orders of magnitude. The measured currents at the first pulse was -8×10^{-11} A and the current after switching was -2×10^{-6} A, which results in an energy consumption of 9×10^{-11}J to $\times10^{-7}$J (90 pJ to 300 nJ per pulse). These results demonstrate that under PVS, we were able to reach a respective energy consumption of $< 3\times10^{-6}$J for $MAPbI_3$ devices and $<3\times10^{-7}$J for PEA_2PbI_4 to induce a switching effect, which is a difference of an order of magnitude. Furthermore, within these measurements, the PEA_2PbI_4 showed a high ON/OFF ratio of $> 10^4$, outperforming $MAPbI_3$ by more than 2 orders of magnitude. An important note is that these measurements were conducted in an exploratory manner to oversee the ON switching effect of the devices with variable pulse times. Much more statistical analysis is needed to provide a suggestion on the reproducibility of these effects. Room for further exploration would be to conduct a measurement range on several interesting parameters like switching the voltage polarities, measuring the conductance over a longer time at a constant voltage bias, and determining subsequent pulses that can actively switch the device ON and OFF. However, optimizing these parameters is difficult as high stress can short the device and low stress can lead to under-performance.

5. Conclusion

In this thesis, we have demonstrated and investigated the resistive switching behaviour in different organic-inorganic MHP structures. By combining the results of the material characterization, IV measurements and PVS measurements, the primary goal of was to shine a light on different organic-inorganic MHP devices for memristive applications, looking at switching behaviour, energy consumption, ON/OFF ratio and endurance. The central comparison was between the 3D perovskite $MAPbI_3$ and the 2D perovskite PEA_2PbI_4. As a result, we observed overall lower currents and potential for higher ON/OFF ratios in PEA_2PbI_4 devices compared to $MAPbI_3$. For $MAPbI_3$, the switching behaviour was gradual and very reproducible over multiple cycles. For PEA_2PbI_4, the switching behaviour was stochastic and took place at different voltages. By deposition of the organic Spiro-OMeTAD hole transport material between the perovskite film and the top gold electrode, we were able to improve the overall ON/OFF ratio and endurance within both device structures. With PVS measurements, we were able to switch the conductivity in the $MAPbI_3$/Spiro device by 2 orders of magnitude with a pulse time of 50 ms, allowing for a energy consumption between 10 nJ to 3μJ per pulse. For the PEA_2PbI_4/Spiro device, the observed conductivity switch was of 4 orders of magnitude with 120 ms pulses, allowing for an energy consumption between 90 pJ-300 nJ per pulse.

From these results, we have successfully acquired a difference in resistive switching behaviour between the $MAPbI_3$ and PEA_2PbI_4 device structures. Due to the smaller carrier mobility and ion mobility in PEA_2PbI_4, overall current through the device decreases by a few orders of magnitude, making 2D perovskites more energy efficient.[22] In the $MAPbI_3$ devices, we attribute the gradual resistive switching behaviour to an interfacial doping mechanism due to ion migration in the perovskite layer. The ON/OFF ratio ($>10^1$) and operating currents ($< 10^{-3}$ A) correspond to the ones displayed for $MAPbI_3$ in literature.[69] In the PEA_2PbI_4 devices, we associate the abrupt changes in conductivity at different voltage magnitudes to come from (partial) filament formation of ion vacancies in the perovskite layer. The potential high ON/OFF ratios ($>10^2$) and stochastic behaviour do not correspond to previous reports of PEA_2PbI_4, where low conductivity is measured for both the ON and the OFF state.[22] The stochastic switching of the PEA_2PbI_4 devices makes accurately setting the conductive state of the device difficult, which is unfavorable for application in artificial synapses. However, stochastically switching devices could be implemented in training probability-based algorithms.[3] Possible reasons for higher ON/OFF ratios due to the addition of the Spiro layer is promotion of conductive filament formation of iodide vacancies and/or doping of the Spiro layer by ions migrating from the perovskite into the organic material. A possible reason for the improved stability of the device is the reduction of reactions

between the migrated iodides and the gold contact at the perovskite/electrode interface. From our results, we have presented that small differences in device configurations can cause large differences in the memristive effect. The results of Spiro-OMeTAD on these perovskite device structures are promising to apply in other perovskite configurations. For instance, further investigation of the influence of a Spiro-OMeTAD transport layer on previously reported perovskite devices with ultralow energy consumption of 400 fJ per pulse.[27] Since we were unable to distinguish the origin of the switching mechanisms in the perovskite devices by IV- and PVS-characteristics alone, more in-depth research into the whole device stack to validate these mechanisms will be necessary.

An outlook for further research would be to verify and expand understanding on the resistive switching mechanisms in the different perovskite structures by 'looking into' the device while poling to the ON/OFF states. First, more in-depth characterization of grain orientation on the surface would be needed, for instance with electron backscatter diffraction (EBSD) measurements. Conductive atomic force microscopy can be used to locally investigate conductivity of the surface, which could provide evidence for conductive filament formation mechanism in the device. Energy disperse X-ray diffraction measurements could give further insight on elemental distribution in the device. This setup could shine light on how ions migrate through the different perovskite structures and if there is any ion migration into the hole-transport layers. As a final outlook, optimized stacks can be implemented in devices with smaller contact areas, which will decrease the current flowing through the device and therefore the energy consumption of the operating memristor. Our findings of using hole-transport materials to optimize the switching effect in perovskite memristors uncover new opportunities. With the insights from this thesis in the back of our mind, research will be able to further develop perovskite memristive devices to reach the femtojoule level of synaptic information transfer in the biological brain.

6. Acknowledgements

I would like to thank a lot of people during my research at AMOLF. First of all, thank you Bruno Ehrler for allowing me to be part of the Hybrid Solar Cells group and for your vast scientific insights on my project. I would also like to thank Erik Garnett for being my examiner for my thesis. My gratitude goes to Jeroen de Boer, who guided me through the first months of my research and taught me a lot about perovskite chemistry and the interesting world of artificial synapses. I would also like to thanks Marc Duursma for doing an amazing job by taking care of our lab. Thanks a lot also to Imme, Moritz and Gianluca for the critical thinking and many scientific insights during my project. I would also like to thank Menke, Kaj, Daan and Georg for the many laughs we had during our time together at Amolf. Thanks also to Karel, Patrick, Cedric and Adrian for the nice talks and music sessions we had as office mates. Finally, thank you to the whole Hybrid Solar Cells group for the great learning environment and enjoyment during my time at AMOLF!

7. References

References

[1] P. Agreement, "Paris agreement," in *Report of the Conference of the Parties to the United Nations Framework Convention on Climate Change (21st Session, 2015: Paris). Retrived December*, vol. 4, p. 2017, HeinOnline, 2015.

[2] M. R. Hannah Ritchie and P. Rosado, "Energy," *Our World in Data*, 2020. https://ourworldindata.org/energy.

[3] H. Bao, H. Zhou, J. Li, H. Pei, J. Tian, L. Yang, S. Ren, S. Tong, Y. Li, Y. He, *et al.*, "Toward memristive in-memory computing: principles and applications," *Frontiers of Optoelectronics*, vol. 15, no. 1, pp. 1–25, 2022.

[4] A. Mehonic, A. Sebastian, B. Rajendran, O. Simeone, E. Vasilaki, and A. J. Kenyon, "Memristors—from in-memory computing, deep learning acceleration, and spiking neural networks to the future of neuromorphic and bio-inspired computing," *Advanced Intelligent Systems*, vol. 2, no. 11, p. 2000085, 2020.

[5] N. Jones *et al.*, "The information factories," *Nature*, vol. 561, no. 7722, pp. 163–6, 2018.

[6] A. S. Andrae and T. Edler, "On global electricity usage of communication technology: trends to 2030," *Challenges*, vol. 6, no. 1, pp. 117–157, 2015.

[7] D. V. Christensen, R. Dittmann, B. Linares-Barranco, A. Sebastian, M. Le Gallo, A. Redaelli, S. Slesazeck, T. Mikolajick, S. Spiga, S. Menzel, *et al.*, "2022 roadmap on neuromorphic computing and engineering," *Neuromorphic Computing and Engineering*, 2022.

[8] M. Zidan, J. Strachan, and W. Lu, "The future of electronics based on memristive systems. nat electron 1 (1): 22–29," 2018.

[9] I. Raifuku, Y. Chao, H. Chen, C. Lin, P. Lin, L. Shih, K. Chen, J. Chen, J. Chen, and P. Chen, "Halide perovskite for low-power consumption neuromorphic devices," *EcoMat*, vol. 3, 12 2021.

[10] G. Indiveri, B. Linares-Barranco, R. Legenstein, G. Deligeorgis, and T. Prodromakis, "Integration of nanoscale memristor synapses in neuromorphic computing architectures," *Nanotechnology*, vol. 24, no. 38, p. 384010, 2013.

[11] D. S. Jeong, K. M. Kim, S. Kim, B. J. Choi, and C. S. Hwang, "Memristors for energy-efficient new computing paradigms," *Advanced Electronic Materials*, vol. 2, no. 9, p. 1600090, 2016.

[12] S. Ambrogio, P. Narayanan, H. Tsai, R. M. Shelby, I. Boybat, C. Di Nolfo, S. Sidler, M. Giordano, M. Bodini, N. C. Farinha, *et al.*, "Equivalent-accuracy accelerated neural-network training using analogue memory," *Nature*, vol. 558, no. 7708, pp. 60–67, 2018.

[13] D. Kuzum, S. Yu, and H. P. Wong, "Synaptic electronics: materials, devices and applications," *Nanotechnology*, vol. 24, no. 38, p. 382001, 2013.

[14] J. Zhu, Y. Yang, R. Jia, Z. Liang, W. Zhu, Z. U. Rehman, L. Bao, X. Zhang, Y. Cai, L. Song, *et al.*, "Ion gated synaptic transistors based on 2d van der waals crystals with tunable diffusive dynamics," *Advanced Materials*, vol. 30, no. 21, p. 1800195, 2018.

[15] C. Zhang, S. Wang, X. Zhao, Y. Yang, Y. Tong, M. Zhang, Q. Tang, and Y. Liu, "Sub-femtojoule-energy-consumption conformable synaptic transistors based on organic single-crystalline nanoribbons," *Advanced Functional Materials*, vol. 31, no. 7, p. 2007894, 2021.

[16] P. C. Harikesh, B. Febriansyah, R. A. John, and N. Mathews, "Hybrid organic-inorganic halide perovskites for scaled-in neuromorphic devices," *MRS Bulletin*, vol. 45, pp. 641–648, 8 2020.

[17] Q. Chen, H. Zhou, Z. Hong, S. Luo, H.-S. Duan, H.-H. Wang, Y. Liu, G. Li, and Y. Yang, "Planar heterojunction perovskite solar cells via vapor-assisted solution process," *Journal of the American Chemical Society*, vol. 136, no. 2, pp. 622–625, 2014.

[18] E. B. Kim, M. S. Akhtar, H. S. Shin, S. Ameen, and M. K. Nazeeruddin, "A review on two-dimensional (2d) and 2d-3d multidimensional perovskite solar cells: Perovskites structures, stability, and photovoltaic performances," 9 2021.

[19] P. Chen, Y. Bai, S. Wang, M. Lyu, J. H. Yun, and L. Wang, "In situ growth of 2d perovskite capping layer for stable and efficient perovskite solar cells," *Advanced Functional Materials*, vol. 28, 4 2018.

[20] H. Zhai, F. Liao, Z. Song, B. Ou, D. Li, D. Xie, H. Sun, L. Xu, C. Cui, and Y. Zhao, "2d pea2pbi4-3d mapbi3composite perovskite interfacial layer for highly efficient and stable mixed-ion perovskite solar cells," *ACS Applied Energy Materials*, vol. 4, pp. 13482–13491, 12 2021.

[21] M. H. Futscher and J. V. Milić, "Mixed conductivity of hybrid halide perovskites: Emerging opportunities and challenges," *Frontiers in Energy Research*, vol. 9, p. 629074, 2021.

[22] A. Solanki, A. Guerrero, Q. Zhang, J. Bisquert, and T. C. Sum, "Interfacial mechanism for efficient resistive switching in ruddlesden-popper perovskites for non-volatile memories," *Journal of Physical Chemistry Letters*, vol. 11, pp. 463–470, 1 2020.

[23] J. H. Heo, D. H. Shin, S. H. Moon, M. H. Lee, D. H. Kim, S. H. Oh, W. Jo, and S. H. Im, "Memory effect behavior with respect to the crystal grain size in the organic-inorganic hybrid perovskite nonvolatile resistive random access memory," *Scientific reports*, vol. 7, no. 1, pp. 1–8, 2017.

[24] J.-M. Yang, E.-S. Choi, S.-Y. Kim, J.-H. Kim, J.-H. Park, and N.-G. Park, "Perovskite-related (ch 3 nh 3) 3 sb 2 br 9 for forming-free memristor and low-energy-consuming neuromorphic computing," *Nanoscale*, vol. 11, no. 13, pp. 6453–6461, 2019.

[25] B. Hwang and J.-S. Lee, "Lead-free, air-stable hybrid organic–inorganic perovskite resistive switching memory with ultrafast switching and multilevel data storage," *Nanoscale*, vol. 10, no. 18, pp. 8578–8584, 2018.

[26] P. Calado, A. M. Telford, D. Bryant, X. Li, J. Nelson, B. C. O'Regan, and P. R. Barnes, "Evidence for ion migration in hybrid perovskite solar cells with minimal hysteresis," *Nature communications*, vol. 7, no. 1, pp. 1–10, 2016.

[27] H. Tian, L. Zhao, X. Wang, Y. W. Yeh, N. Yao, B. P. Rand, and T. L. Ren, "Extremely low operating current resistive memory based on exfoliated 2d perovskite single crystals for neuromorphic computing," *ACS Nano*, vol. 11, pp. 12247–12256, 12 2017.

[28] B. Barbour, N. Brunel, V. Hakim, and J.-P. Nadal, "What can we learn from synaptic weight distributions?," *TRENDS in Neurosciences*, vol. 30, no. 12, pp. 622–629, 2007.

[29] D. Marković, A. Mizrahi, D. Querlioz, and J. Grollier, "Physics for neuromorphic computing," *Nature Reviews Physics*, vol. 2, no. 9, pp. 499–510, 2020.

[30] M. Hu, J. P. Strachan, Z. Li, E. M. Grafals, N. Davila, C. Graves, S. Lam, N. Ge, J. J. Yang, and R. S. Williams, "Dot-product engine for neuromorphic computing: Programming 1t1m crossbar to accelerate matrix-vector multiplication," in *2016 53nd acm/edac/ieee design automation conference (dac)*, pp. 1–6, IEEE, 2016.

[31] M. Zhao, B. Gao, J. Tang, H. Qian, and H. Wu, "Reliability of analog resistive switching memory for neuromorphic computing," *Applied Physics Reviews*, vol. 7, no. 1, p. 011301, 2020.

[32] D. B. Strukov, G. S. Snider, D. R. Stewart, and R. S. Williams, "The missing memristor found," *Nature*, vol. 453, pp. 80–83, 5 2008.

[33] A. Chanthbouala, V. Garcia, R. O. Cherifi, K. Bouzehouane, S. Fusil, X. Moya, S. Xavier, H. Yamada, C. Deranlot, N. D. Mathur, *et al.*, "A ferroelectric memristor," *Nature materials*, vol. 11, no. 10, pp. 860–864, 2012.

[34] S. Park, H. Kim, M. Choo, J. Noh, A. Sheri, S. Jung, K. Seo, J. Park, S. Kim, W. Lee, *et al.*, "Rram-based synapse for neuromorphic system with pattern recognition function," in *2012 international electron devices meeting*, pp. 10–2, IEEE, 2012.

[35] S. Park, A. Sheri, J. Kim, J. Noh, J. Jang, M. Jeon, B. Lee, B. Lee, B. Lee, and H. Hwang, "Neuromorphic speech systems using advanced reram-based synapse," in *2013 IEEE International Electron Devices Meeting*, pp. 25–6, IEEE, 2013.

[36] S. Yu and H.-S. P. Wong, "Modeling the switching dynamics of programmable-metallization-cell (pmc) memory and its application as synapse device for a neuromorphic computation system," in *2010 International Electron Devices Meeting*, pp. 22–1, IEEE, 2010.

[37] D. Kuzum, R. G. Jeyasingh, and H.-S. P. Wong, "Energy efficient programming of nanoelectronic synaptic devices for large-scale implementation of associative and temporal sequence learning," in *2011 International Electron Devices Meeting*, pp. 30–3, IEEE, 2011.

[38] T. Serrano-Gotarredona, T. Masquelier, T. Prodromakis, G. Indiveri, and B. Linares-Barranco, "Stdp and stdp variations with memristors for spiking neuromorphic learning systems," *Frontiers in Neuroscience*, 2013.

[39] S. Srivastava, J. P. Thomas, N. F. Heinig, and K. Leung, "High-performance single-active-layer memristor based on an ultrananocrystalline oxygen-deficient tio x film," *ACS applied materials & interfaces*, vol. 9, no. 42, pp. 36989–36996, 2017.

[40] O. A. Olumodeji and M. Gottardi, "A pulse-based memristor programming circuit," in *2017 IEEE International Symposium on Circuits and Systems (ISCAS)*, pp. 1–4, 2017.

[41] Y. Park and J.-S. Lee, "Metal halide perovskite-based memristors for emerging memory applications," *The Journal of Physical Chemistry Letters*, vol. 13, pp. 5638–5647, 2022.

[42] X. Xiao, J. Hu, S. Tang, K. Yan, B. Gao, H. Chen, and D. Zou, "Recent advances in halide perovskite memristors: materials, structures, mechanisms, and applications," *Advanced Materials Technologies*, vol. 5, no. 6, p. 1900914, 2020.

[43] K. Yan, M. Peng, X. Yu, X. Cai, S. Chen, H. Hu, B. Chen, X. Gao, B. Dong, and D. Zou, "High-performance perovskite memristor based on methyl ammonium lead halides," *Journal of Materials Chemistry C*, vol. 4, no. 7, pp. 1375–1381, 2016.

[44] M. A. Green, A. Ho-Baillie, and H. J. Snaith, "The emergence of perovskite solar cells," *Nature photonics*, vol. 8, no. 7, pp. 506–514, 2014.

[45] E. Bi, Z. Song, C. Li, Z. Wu, and Y. Yan, "Mitigating ion migration in perovskite solar cells," 7 2021.

[46] F. Bella, P. Renzi, C. Cavallo, and C. Gerbaldi, "Caesium for perovskite solar cells: An overview," 8 2018.

[47] S. I. Kim, Y. Lee, M. H. Park, G. T. Go, Y. H. Kim, W. Xu, H. D. Lee, H. Kim, D. G. Seo, W. Lee, and T. W. Lee, "Dimensionality dependent plasticity in halide perovskite artificial synapses for neuromorphic computing," *Advanced Electronic Materials*, vol. 5, 9 2019.

[48] S. Thiyagu, C. C. Hsueh, C. T. Liu, H. J. Syu, T. C. Lin, and C. F. Lin, "Hybrid organic-inorganic heterojunction solar cells with 12utilizing flexible film-silicon with a hierarchical surface," *Nanoscale*, vol. 6, pp. 3361–3366, 3 2014.

[49] C. C. Stoumpos, D. H. Cao, D. J. Clark, J. Young, J. M. Rondinelli, J. I. Jang, J. T. Hupp, and M. G. Kanatzidis, "Ruddlesden-popper hybrid lead iodide perovskite 2d homologous semiconductors," *Chemistry of Materials*, vol. 28, pp. 2852–2867, 5 2016.

[50] M. H. Futscher, J. M. Lee, L. McGovern, L. A. Muscarella, T. Wang, M. I. Haider, A. Fakharuddin, L. Schmidt-Mende, and B. Ehrler, "Quantification of ion migration in ch3nh3pbi3 perovskite solar cells by transient capacitance measurements," *Materials Horizons*, vol. 6, pp. 1497–1503, 8 2019.

[51] J. M. Azpiroz, E. Mosconi, J. Bisquert, and F. De Angelis, "Defect migration in methylammonium lead iodide and its role in perovskite solar cell operation," *Energy & Environmental Science*, vol. 8, no. 7, pp. 2118–2127, 2015.

[52] J. Haruyama, K. Sodeyama, L. Han, and Y. Tateyama, "First-principles study of ion diffusion in perovskite solar cell sensitizers," *Journal of the American Chemical Society*, vol. 137, no. 32, pp. 10048–10051, 2015.

[53] S. Meloni, T. Moehl, W. Tress, M. Franckevičius, M. Saliba, Y. H. Lee, P. Gao, M. K. Nazeeruddin, S. M. Zakeeruddin, U. Rothlisberger, *et al.*, "Ionic polarization-induced current–voltage hysteresis in ch3nh3pbx3 perovskite solar cells," *Nature communications*, vol. 7, no. 1, pp. 1–9, 2016.

[54] C. Eames, J. M. Frost, P. R. Barnes, B. C. O'Regan, A. Walsh, and M. S. Islam, "Ionic transport in hybrid lead iodide perovskite solar cells," *Nature Communications*, vol. 6, 6 2015.

[55] D. Meggiolaro, E. Mosconi, and F. D. Angelis, "Formation of surface defects dominates ion migration in lead-halide perovskites," *ACS Energy Letters*, vol. 4, pp. 779–785, 3 2019.

[56] Y. Shao, Y. Fang, T. Li, Q. Wang, Q. Dong, Y. Deng, Y. Yuan, H. Wei, M. Wang, A. Gruverman, J. Shield, and J. Huang, "Grain boundary dominated ion migration in polycrystalline organic-inorganic halide perovskite films," *Energy and Environmental Science*, vol. 9, pp. 1752–1759, 5 2016.

[57] J. S. Yun, J. Seidel, J. Kim, A. M. Soufiani, S. Huang, J. Lau, N. J. Jeon, S. I. Seok, M. A. Green, and A. Ho-Baillie, "Critical role of grain boundaries for ion migration in formamidinium and methylammonium lead halide perovskite solar cells," *Advanced Energy Materials*, vol. 6, no. 13, p. 1600330, 2016.

[58] L. McGovern, I. Koschany, G. Grimaldi, L. A. Muscarella, and B. Ehrler, "Grain size influences activation energy and migration pathways in mapbbr3 perovskite solar cells," *The journal of physical chemistry letters*, vol. 12, no. 9, pp. 2423–2428, 2021.

[59] E. Koren, E. Lörtscher, C. Rawlings, A. W. Knoll, and U. Duerig, "Adhesion and friction in mesoscopic graphite contacts," *Science*, vol. 348, pp. 679–683, 5 2015.

[60] Z. Huang, A. H. Proppe, H. Tan, M. I. Saidaminov, F. Tan, A. Mei, C.-S. Tan, M. Wei, Y. Hou, H. Han, *et al.*, "Suppressed ion migration in reduced-dimensional perovskites improves operating stability," *ACS Energy Letters*, vol. 4, no. 7, pp. 1521–1527, 2019.

[61] J. Xing, Q. Wang, Q. Dong, Y. Yuan, Y. Fang, and J. Huang, "Ultrafast ion migration in hybrid perovskite polycrystalline thin films under light and suppression in single crystals," *Physical Chemistry Chemical Physics*, vol. 18, no. 44, pp. 30484–30490, 2016.

[62] X. Zhao, H. Xu, Z. Wang, Y. Lin, and Y. Liu, "Memristors with organic-inorganic halide perovskites," 6 2019.

[63] N. N. Shlenskaya, N. A. Belich, M. Grätzel, E. A. Goodilin, and A. B. Tarasov, "Light-induced reactivity of gold and hybrid perovskite as a new possible degradation mechanism in perovskite solar cells," *Journal of Materials Chemistry A*, vol. 6, no. 4, pp. 1780–1786, 2018.

[64] Z. Xiao, Y. Yuan, Y. Shao, Q. Wang, Q. Dong, C. Bi, P. Sharma, A. Gruverman, and J. Huang, "Giant switchable photovoltaic effect in organometal trihalide perovskite devices," *Nature Materials*, vol. 14, pp. 193–197, 2015.

[65] Z. Xiao and J. Huang, "Energy-efficient hybrid perovskite memristors and synaptic devices," *Advanced Electronic Materials*, vol. 2, 7 2016.

[66] X. Guan, W. Hu, M. A. Haque, N. Wei, Z. Liu, A. Chen, and T. Wu, "Light-responsive ion-redistribution-induced resistive switching in hybrid perovskite schottky junctions," *Advanced Functional Materials*, vol. 28, 1 2018.

[67] Y. Huang, Z. Zhao, C. Wang, H. Fan, Y. Yang, J. Bian, and H. Wu, "Conductive metallic filaments dominate in hybrid perovskite-based memory devices," *Science China Materials*, vol. 62, no. 9, pp. 1323–1331, 2019.

[68] S. M. Lee, H. Kim, D. H. Kim, W. B. Kim, J. M. Lee, J. Choi, H. Shin, G. S. Han, H. W. Jang, and H. S. Jung, "Tailored 2d/3d halide perovskite heterointerface for substantially enhanced endurance in conducting bridge resistive switching memory," *ACS Applied Materials and Interfaces*, vol. 12, pp. 17039–17045, 4 2020.

[69] Y. Ren, H. Ma, W. Wang, Z. Wang, H. Xu, X. Zhao, W. Liu, J. Ma, and Y. Liu, "Cycling-induced degradation of organic–inorganic perovskite-based resistive switching memory," *Advanced Materials Technologies*, vol. 4, no. 1, p. 1800238, 2019.

[70] X. Zhu, J. Lee, and W. D. Lu, "Iodine vacancy redistribution in organic–inorganic halide perovskite films and resistive switching effects," *Advanced Materials*, vol. 29, no. 29, p. 1700527, 2017.

[71] S. Li, Y. L. Cao, W. H. Li, and Z. S. Bo, "A brief review of hole transporting materials commonly used in perovskite solar cells," 10 2021.

[72] J. Zhang, L. Xu, P. Huang, Y. Zhou, Y. Zhu, N. Yuan, J. Ding, Z. Zhang, and Y. Li, "A simple and dopant-free hole-transporting material based on (2-ethylhexyl)-9 h-carbazole for efficient planar perovskite solar cells," *Journal of Materials Chemistry C*, vol. 5, no. 48, pp. 12752–12757, 2017.

[73] M. Girish, *Monodisperse Gold Nanoparticles: Synthesis, Self-Assembly and Fabrication of Floating Gate Memory Devices*. PhD thesis, 2018.

[74] C. Song, H. Yang, F. Liu, and G. J. Cheng, "Ultrafast femtosecond pressure modulation of structure and exciton kinetics in 2d halide perovskites for enhanced light response and stability," *Nature Communications*, vol. 12, no. 1, pp. 1–9, 2021.

[75] P. Basumatary and P. Agarwal, "Photocurrent transient measurements in mapbi3 thin films," *Journal of Materials Science: Materials in Electronics*, vol. 31, pp. 10047–10054, 7 2020.

[76] M. G. La-Placa, D. Guo, L. Gil-Escrig, F. Palazon, M. Sessolo, and H. J. Bolink, "Dual-source vacuum deposition of pure and mixed halide 2d perovskites: Thin film characterization and processing guidelines," *Journal of Materials Chemistry C*, vol. 8, pp. 1902–1908, 2 2020.

[77] L. A. Muscarella, E. M. Hutter, S. Sanchez, C. D. Dieleman, T. J. Savenije, A. Hagfeldt, M. Saliba, and B. Ehrler, "Crystal orientation and grain size: do they determine optoelectronic properties of mapbi3 perovskite?," *The journal of physical chemistry letters*, vol. 10, no. 20, pp. 6010–6018, 2019.

8. Appendix

8.1. Bottom layers characterization

Figure 8.1a shows a 1 by 1 μm top AFM image of an ITO substrate. Figure 8.1b shows a 1 by 1 μm top AFM image of a spincoated PTAA thin film on top of an ITO substrate. The image looks very similar to the ITO morphology, which gives an indication that the layer might be very thin. Therefore, we have scratched a trench in the PTAA with a toothpick and measured the height difference between the PTAA and the ITO in Figure 8.2. From this image, we can see clear difference of around 5-10 nm, resulting in the measured thickness of the PTAA thin film.

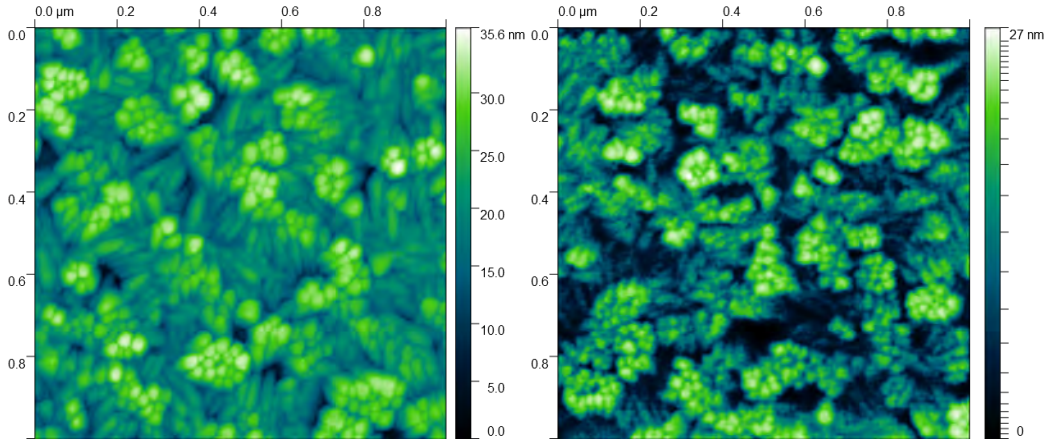

Fig. 8.1: a) 1 by 1 μm top AFM image of an ITO substrate. b) 1 by 1 μm top AFM image of a spincoated PTAA thin film on top of ITO.

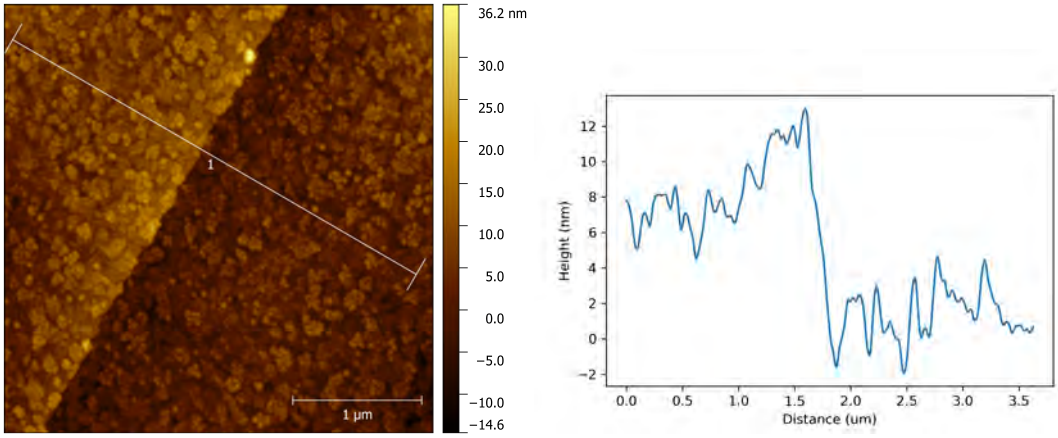

Fig. 8.2: a) 3 by 3 μm top AFM image of a PTAA thin film on top of the ITO substrate. The left side of the AFM image is the PTAA, where the right side (darker brown) is the trench in the film. b) a plot of the linescan in a), where the height difference over distance is presented.

8.2. Spiro-OMeTAD top layer characterization

Figure 8.3 shows the AFM images of Spiro-OMeTAD on the perovskite layers. For Spiro-OMeTAD on $MAPbI_3$, this RMS roughness is 0.96 nm. The RMS roughness within the scanned 1 by 1 μm area for Spiro-OMeTAD on PEA_2PbI_4 is of 0.94 nm. This indicates that the deposition of the Spiro film on top of the perovskite results in a smooth surface which fully covers the substrate.

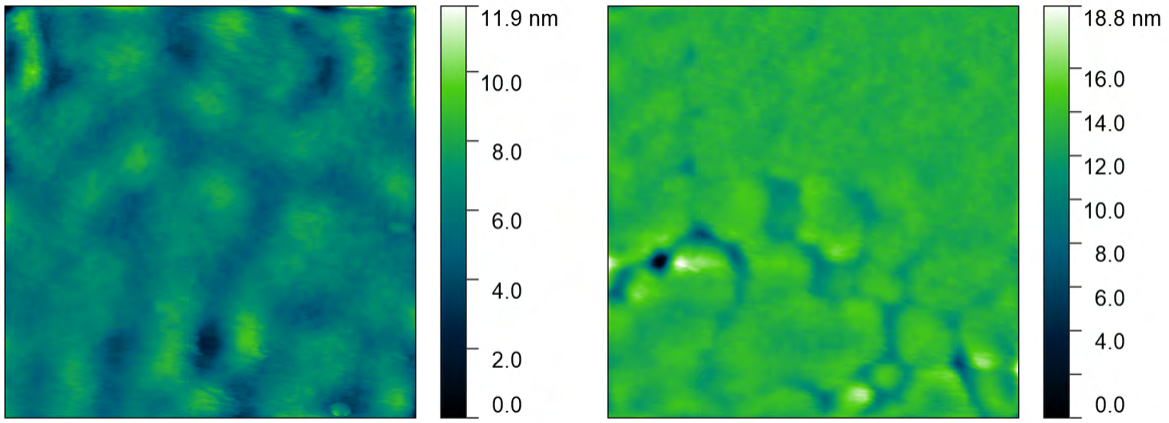

Fig. 8.3: a) 1 x 1 μm AFM images of a Spiro-OMeTAD thin film deposited on $MAPbI_3$. RMS roughness is 0.96 nm. b) 1 x 1 μm AFM images of a Spiro-OMeTAD thin film deposited on PEA_2PbI_4. RMS roughness is 0.94 nm.

8.3. Extra IV sweeps

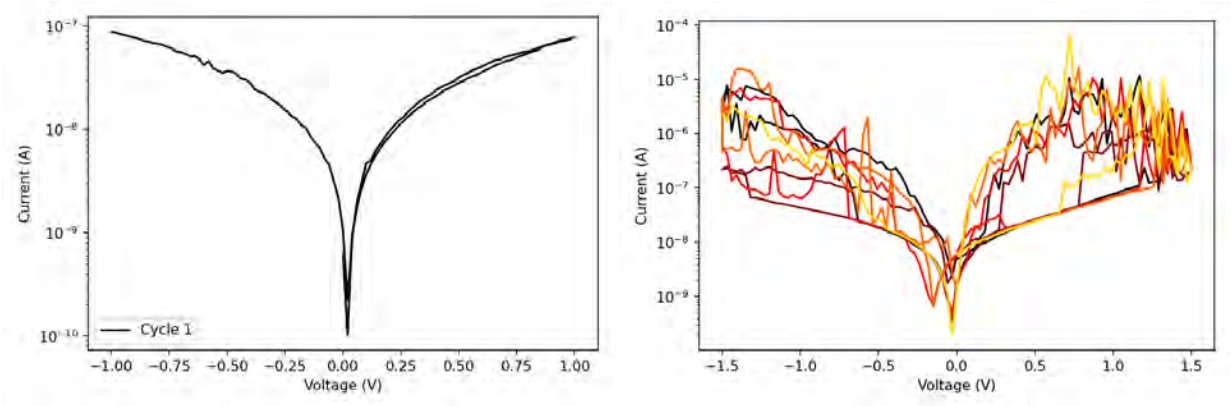

Fig. 8.4: a) Typical IV sweep of a PEA_2PbI_4 device between -1V and +1V, where no hysteresis was measured. b) 5 subsequent IV sweeps of a PEA_2PbI_4 device between -1.5V and +1.5V.

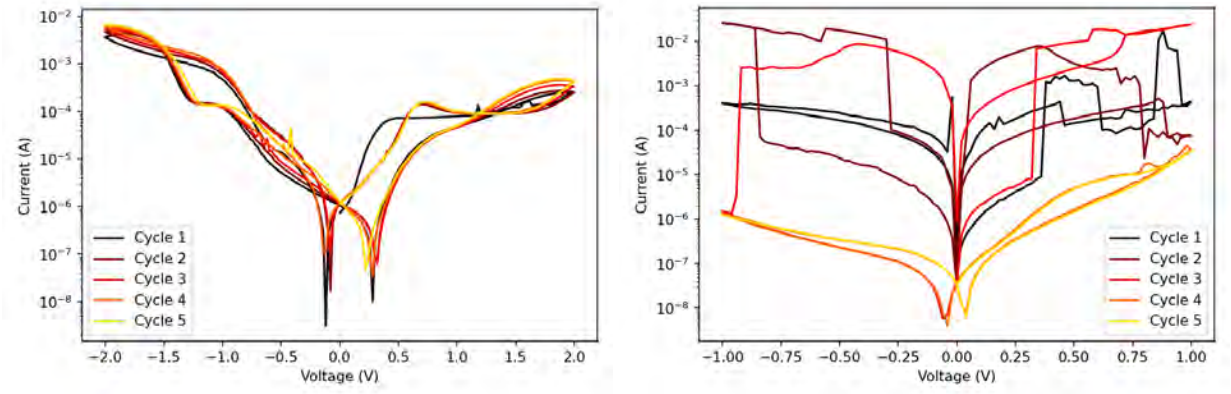

Fig. 8.5: a) Typical IV sweep of $MAPbI_3$ device between -2V and +2V, showing no extra hysteresis effect over higher voltages. b) IV sweep of $MAPbI_3$/Spiro-OMeTAD device between -1 and +1V, which shows stochastic switching at low voltages. This greatly differs that greatly differs from normal $MAPbI_3$ devices.

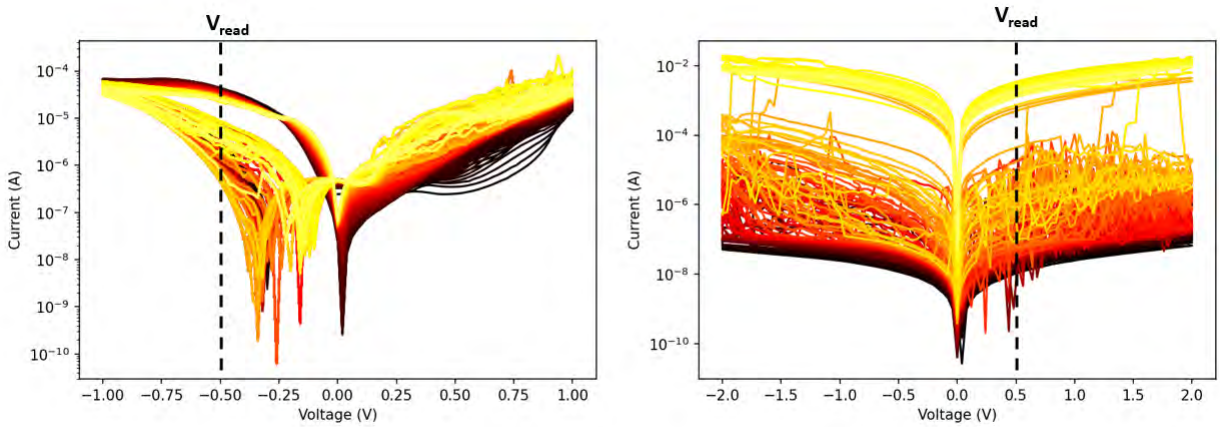

Fig. 8.6: a) 100 subsequent IV sweeps of $MAPbI_3$, V_{read} = -0.5V. b) 100 subsequent IV sweeps of PEA_2PbI_4, V_{read} = +0.5V.

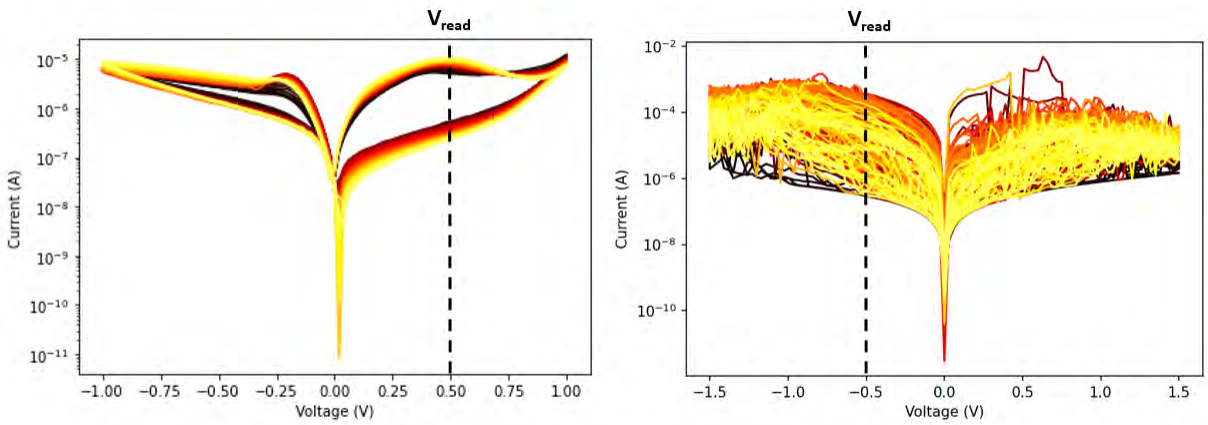

Fig. 8.7: a) 100 subsequent IV sweeps of $MAPbI_3$/Spiro, V_{read} = +0.5V. b) 100 subsequent IV sweeps of PEA_2PbI_4/Spiro, V_{read} = -0.5V.